Journal of Wind Engineering & Industrial Aerodynamics 214 (2021) 104677

Contents lists available at ScienceDirect

Journal of Wind Engineering & Industrial Aerodynamics

journal homepage: www.elsevier.com/locate/jweia

Atmospheric transport over open-pit mines: The effects of thermal stability and mine depth

Seyedahmad Kia [a], Thomas K. Flesch [b], Brian S. Freeman [c], Amir A. Aliabadi [a,*]

[a] School of Engineering, University of Guelph, Guelph, ON, Canada
[b] Department of Earth and Atmospheric Sciences, University of Alberta, Edmonton, AB, Canada
[c] Lakes Environmental, Waterloo, ON, Canada

ARTICLE INFO

Keywords:
Atmospheric transport
Computational fluid dynamics (CFD)
Open-pit mines
Thermal stability
Turbulence

ABSTRACT

A key difficulty in air pollution dispersion modeling and quantifying fugitive emission fluxes of pollutants from open-pit mines is that the meteorological fields for such complex terrains cannot be reliably predicted using simplistic surface layer theory. In this study, transport phenomena over a shallow (100 m) and a deep (500 m) synthetic mine are predicted under thermally unstable, neutral, and stable conditions using CFD modelling. The skimming flow is only predicted under the neutral case, while more complex flow patterns emerge otherwise. Under the unstable case, the shallow and deep mines induce enhanced mixing downstream of the mine, resulting in substantial vertical plume transport and dilution of the pollutants released from the mine. Under the stable case, the plume from the shallow mine is restricted to the surface layer downstream of the mine. However, under the stable case, the plume from the deep mine rises into the substantial portion of the boundary layer due to formation of a standing wave over and inside the mine. The results suggest that the CFD model can predict transport phenomena over open-pit mines reliably, so that the meteorological fields may be incorporated in operational models to improve accuracy of their predictions.

1. Introduction

The extraction of minerals from an open-pit in the ground is a surface mining procedure called open-pit mining. The surface mining technique can be used when mineral or ore deposits are close to the surface of the earth. Mining activities often create large fugitive dust and greenhouse gases from the extraction, so it is crucial to understand atmospheric transport processes inside and near open-pit mines carefully. The open-pit mine is completely different from the usually studied valleys formed from fluvial or glacial activity. Air circulations, shear layers, and meandering can be created as a result of the existence of an open-pit terrain (Silvester et al., 2009). The ventilation of open-pit depends on the wind flow characteristics induced by the mine pit (Silvester et al., 2009; Flores et al., 2014; Bhowmick et al., 2015). Many studies measured and analyzed the amount of dust, volatile organic compounds, greenhouse gases, and polycyclic aromatic compounds released from open pits (Gordon et al., 2015; Li et al., 2017; Baray et al., 2018; Qiu et al., 2018; Liggio et al., 2019; Katta et al., 2020; Nambiar et al., 2020b; Rodovalho et al., 2020).

Natural topographical examples similar to the depression of an open-pit mine are the Arizona's Meteor Crater (Whiteman et al., 2008; Lehner et al., 2016), Peter Sinks in Utah (Clements et al., 2003), and the Gruenloch doline in Austria (Whiteman et al., 2004), all of which have been investigated in detail. Meteorological characteristics of such depressions are different from those of homogeneous flat terrain and valleys. For example, a temperature-stratified, quiescent, and cool pool of air forms at the bottom of such depressions under thermally stable conditions during the night (Clements et al., 2003; Whiteman et al., 2004, 2008, 2008; Lehner et al., 2016). In comparison to flat terrain and valleys, the meteorological features inside the depression exhibit reduced slope flows, reduced advective transfer with air outside of the depression, reduced turbulent sensible heat flux at the bottom surface of the depression, change of wind direction from the cool pool to altitudes outside the depression, and formation of weak and intermittent turbulent jets on the depression walls near the ground (Clements et al., 2003; Whiteman et al., 2004). Also, standing waves or oscillating temperature fields have been observed in such depressions, and the temperature stratification is noted to disintegrate under high wind conditions

* Corresponding author.
E-mail address: aliabadi@uoguelph.ca (A.A. Aliabadi).
URL: http://www.aaa-scientists.com (A.A. Aliabadi).

https://doi.org/10.1016/j.jweia.2021.104677
Received 5 October 2020; Received in revised form 14 March 2021; Accepted 17 May 2021
0167-6105/© 2021 Elsevier Ltd. All rights reserved.

(Whiteman et al., 2008; Lehner et al., 2016). The meteorological conditions of such depressions are understood to be influenced by synoptic events, seasonal weather variation, topography, and radiative heat transfer between the depression and the sky, which is a function of depression aspect ratio (Clements et al., 2003; Whiteman et al., 2004). It is informative to study if open-pit mines exhibit similar meteorological conditions, particularly given the confounding influence of nearby industrial operations.

Open-pit mines are used when deposits of commercially useful minerals or rocks are found near the surface. For example, most oil sand mines are categorized as shallow open-pit mines of less than 100-m depth. Deep open-pit mines can be used in coal mining and hard rock mining for ores such as copper, gold, iron, aluminum, and many other minerals. These kinds of mines are deeper than oil sand mines with more than a few hundred meters in depth. To prevent and minimize damage and danger from rock falls, the walls of the pit are generally dug on an angle less than vertical. This design angle depends on how weathered the rocks are, the type of rock, and also how many structural weaknesses occur within the rocks, such as faults, shears, joints, or foliations. At the side of the pit, a haul road is situated, forming a ramp to let trucks drive, carrying ore and waste rock.

In designing the mine walls, typically the maximum ramp height is 12 m. A minimum 1-lane road width would be twice a truck width plus two windrow widths; a minimum 2-lane road would be 3.5 time a truck width plus two windrow widths. For a Komatsu 830e haul truck (7.3 m wide) this suggests a ramp of 25 m wide and 10 m tall (single road) or 40 m wide and 10 m tall (double road). The bench width can vary between 3 and 30 m depending on the mine type and the overall slope angle of the wall. For example, for an oil sand mine, the bench face angle can be changed from 20° to 30° resulting in a bench width of approximately 10 m.

The prediction of wind field over complex terrains, such as an open-pit mine, are usually based on the numerical solution of the Navier-Stokes transport equations and a turbulence model in a domain that includes the local terrain (Kim et al., 2000). In the 1990s and early 2000s Baklanov (1995, 2000) was the first to propose the need to approach the atmospheric transport problem over open-pit mines from a multi-physics perspective, highlighting the combination of scales involved and the importance of topography. The limitation of the availability of observation platforms and the difficulty in acquiring data from complex environments have resulted in atmospheric turbulence studies to only focus on relatively smooth terrain and horizontally homogeneous environments (Kato and Hanafusa, 1996; Maurer et al., 2016; Han et al., 2016; Aliabadi et al., 2018). However, the study of the Atmospheric Boundary Layer (ABL) and surface-atmosphere interaction over complex terrain is significant for many applications. Horizontal gradients of momentum or temperature can be formed by surface heterogeneity, which influence or complicate the horizontal and vertical transport mechanisms, for instance by slope flows or thermals (Mahrt and Vickers, 2005; Medeiros and Fitzjarrald, 2014; Nahian et al., 2020). The established model parameterizations of turbulent processes for atmospheric flows over smooth and homogeneous surfaces often fail to be applied over complex terrain successfully (Roth, 2000).

Numerical simulation technology is increasingly being employed to give advanced warning of potential air quality problems as a result of open-pit mining emissions in addition to providing a basis for future planning of activities. The initial entrainment and subsequent dispersion of fugitive dust and other pollutants present a process complicated by the combination of the in-pit topography, the surrounding natural topography, and the dynamic nature of emissions from these sites (Silvester et al., 2009).

There is growing interest in applying Computational Fluid Dynamics (CFD) to simulate complex micro-meteorological processes inside and around open-pit mines. In general, the problem can be described in terms of the interaction, within the ABL, between the atmosphere and the objects that define the complex surface geometry (Flores et al., 2013). In high-resolution numerical modeling, equations of the transportation of mass, momentum, energy, and atmospheric species are solved to predict the future time evolution of the atmosphere or alternatively reconstruct a past state of the atmosphere at high resolution for detailed investigation of transport phenomena. The computational cost of CFD is dropping as a result of the increasing speed of computers, so the amount of physical experimentation can be reduced considerably by running CFD models instead. Not only can CFD be used to conduct virtual experiments, it can also be used to design physical experiments better with increased efficiency (Xu et al., 2017). There have been many modeling efforts to understand the turbulence structure of ABL using various numerical techniques.

While Direct Numerical Simulations (DNS) are too computationally expensive, and Reynolds-Averaged Navier-Stokes (RANS) or eddy viscosity models suffer from lack of accuracy, Large-Eddy Simulations (LES) have been used as a useful alternative numerical tool to simulate the ABL with sufficient reliability (Aliabadi et al., 2018). In LES, the turbulent eddies of the size of the computational grid cells and larger are explicitly resolved, while the effects of the smaller eddies on the large ones and the mean flow field are parameterized using Sub-Grid Scale (SGS) models (Kumar et al., 2006). LES is able to simulate explicitly the complex flows and turbulence structures in ABL in a transient manner. Its results can be used to complement field measurements and laboratory observations in order to enrich the fundamental understanding of atmospheric transport processes (Cheng and Liu, 2011). In low-Reynolds number or highly thermally-stable flows, LES can predict the unsteady variation in flow and concentration fields more accurately than RANS models (Lin et al., 2021). This superiority stems from the fact that LES resolves large scales of turbulence that may be the driving forces for pollutant dispersion. Therefore, it can provide reliable results in a wider range of flows and applications. Complex terrains with topographical changes may induce slope flows, flow separations, and re-circulations, which can be simulated more successfully using the LES method (Flores et al., 2014). In addition to the numerical techniques used in hybrid LES methods, Very Large-Eddy Simulation (VLES) is another powerful tool to economize the CFD simulations. The concept of VLES, originally proposed by Speziale (1998) is one of the earliest hybrid CFD methods. The main distinction between VLES and the standard LES is the determination of filter width with respect to the grid size. In pure LES, the filter width is associated with the grid size, while the filter width in VLES can be set arbitrarily at any value between the grid size and the large characteristic length-scales of the flow (Labois and Lakehal, 2011; Thé and Yu, 2017). Increasing the filter width will reduce the computational cost of the model at the cost of accuracy. Based on this definition, the VLES becomes LES when the filter width is set as its lowest limit of grid size. Pope (2000) proposed a numerical definition for the distinction between LES and VLES. According to Pope (2000), an LES with a sufficiently fine grid and filter length should resolve more than 80% of the Turbulence Kinetic Energy (TKE) everywhere in the domain except near-wall regions where wall treatments may be used. In contrast, the VLES is defined as a method with coarse grid size and filter length that would resolve possibly less than 80% of the TKE in the domain.

The airflow over complex terrains such as mountains, valleys, and cavities have been studied to investigate the processes of natural ventilation. Baklanov (1995) developed a numerical spatial model of turbulent dynamics of the atmosphere over complex topography to perform atmospheric transport simulations over an open-pit area using LES with an SGS model closure of Smagorinsky-Deardorff. Their study aimed to demonstrate the wind flow and the open-pit-atmosphere interaction under various thermal stability conditions. They predicted formation of tear-off currents, circulation zones, and thermals. In another study, Brés and Colonius (2008) characterized two- and three-dimensional global instabilities of compressible flow over open cavities using a DNS method. They considered cavities that were homogeneous in the span-wise direction. Their results indicated that the

instabilities were hydrodynamic (rather than acoustic) in nature and arose from a generic centrifugal instability mechanism associated with the mean recirculating vortical flow in the downstream part of the cavity. Kang and Sung (2009) performed Particle Image Velocimetry (PIV) measurements and Proper Orthogonal Decomposition (POD) analysis in turbulent flows over a laboratory-scale open cavity to characterize large-scale vortical structures responsible for self-sustained oscillations. Ghoreishi-Madiseh et al. (2017) developed a three-dimensional unsteady Local Thermal Non-Equilibrium (LTNE) CFD model to evaluate thermal storage and heat transfer between ventilation air and a rock pit. Their results suggested that the seasonal thermal energy storage of the rock pit could assist thermal management in an underground mine and could reduce energy consumption for winter heating and summer cooling. Shi et al. (2000) used a high-resolution three-dimensional non-hydrostatic CFD model to simulate the air circulation inside a 2-km wide and 100-m deep open-pit mine. They were able to predict the air circulation inside the cavity, which was responsible for the dilution of pollutants inside the pit. Their results showed that both mechanical and thermal forcing were important mechanisms controlling the evolution of the atmosphere inside the pit. Silvester et al. (2009) used a CFD code based on the standard $k-\varepsilon$ RANS turbulence model to study the mechanically-forced circulations developed inside the Old Moor open-pit (1-km wide and 650-m deep). They showed that the interaction of the wind sweeping over the cavity and the internal atmosphere caused strong mechanical shear near the top of the pit. Choudhury and Bandopadhyay (2016) applied a three-dimensional numerical simulation to model the flow of air and the transport of gaseous pollutants in an Arctic open-pit mine and investigated the effects of low and high wind speeds on the pollutants' profiles in the mine. They showed that while higher velocities of air could remove the pollutants from the pit bottom, they could not remove pollutants from the pit entirely, which necessitated artificial mitigation measures.

In general, most CFD studies have considered the case of a thermally neutral (not vertically stratified) ambient atmosphere. However, thermal stability has been seen to have a strong influence over flow features in complex topography. Bhowmick (2015) used CFD to estimate the fugitive dust retention in two idealized open-pit domains for various weather conditions in a clear sky. The domains were simulated for both summer and winter weather conditions in a high-latitude Arctic and a sub-Arctic open-pit mine. The RANS method with a standard k-ε turbulence model was used to simulate the fugitive dust transport in the pits. The results showed that the combined effect of mechanical and thermal (surface heat flux) forcing during summer conditions cleared the fugitive dust from the open-pit mine within 1 h. However, in winter, the negative heat flux from the pit surface often lead to an atmospheric inversion in the open-pit domain, which resulted in extensive retention of fugitive dust for a prolonged duration. Tukkaraja et al. (2016) simulated the air temperature inversion conditions in a hypothetical open-pit mine using CFD with a RANS method based on the k-ε turbulence model and investigated the effect of the temperature inversion on the dispersion of gas and dust particles in the pit. They showed that the gas and dust particles were trapped inside the pit under inversion conditions while they were dispersed in the absence of inversion. Joseph et al. (2018) studied two distinct open-pit mines for an artificial and an actual terrain using CFD. They presented an evaluation of a buoyancy-modified k-ε dust dispersion model for predicting fugitive dust deposition from a surface quarry. The dust clouds were modeled as volumetric emission, and their dispersion were simulated by coupling the flow field with stochastic tracking of the particulates. They concluded that 1) the in-pit deposition is underestimated without a realistic flow field, 2) CFD models of thermally neutral condition are not sufficient, requiring analysis of thermally unstable and stable conditions, and 3) in-pit topography and surrounding terrain must be considered.

Some studies simulated the idealized terrain to show the advantages and disadvantages of simplified geometry. The LES method by Bhowmick (2015) showed that the idealized pits had several advantages over the actual pits: idealized domains contained no faceted topography due to simplified geometry; mesh quality in numerical simulations was better due to the absence of vertices and ridges; acceptable resolution in the solution could be achieved with higher grid density compared to an actual pit domain due to a planar pit surface; less number of mesh elements were needed; and statistically stationary flow conditions were reached more quickly than the simulation for the actual pit. Flores et al. (2014) performed a Detached Eddy Simulation (DES), which combines the LES in the domain interior, to resolve large atmospheric eddies, with the RANS method near walls, to model transport phenomena near walls, using the Open Fields Operations and Manipulation (OpenFOAM) CFD simulation package to simulate and predict particle dispersion in an idealized mine and an actual open-pit mine in Chile. The idealized pit, which was a simplified topography, retained the same general dimensions of the Chuquicamata copper mine, but it represented the pit as an inverted truncated cone with a superior diameter of 4 km, an interior diameter of 1 km, and a depth of 1 km. The simulations were performed for three different conditions: 1) thermally neutral condition: air advection with mean wind speed of 10 m s^{-1} driving mechanical turbulence under isothermal conditions; 2) thermal buoyancy driven condition: air advection with mean wind speed of 1 m s^{-1} driving mechanical turbulence with surface vertical sensible heat flux of 240 W m^{-2} driving thermal buoyancy; and 3) thermally unstable condition: both air advection (10 m s^{-1}) and surface heat flux (240 W m^{-2}) being considered. The results showed that the buoyant currents contributed to the removal of a large percentage of the particles.

1.1. Objectives

This work focuses on the development of a CFD model for wind flow and dispersion of area-fugitive gas pollutants for open-pit mines. In previous studies, the simulation of over-simplified open-pits (e.g. in the form of a cylinder or inverted cone) was conducted over shallow or deep mines, while more realistic mine geometries (e.g. kidney shape) and variation in mine depth were overlooked. Thermal stability conditions appear to play a significant role in forming flow fields and defining the complexity of the flow pattern inside and surrounding the pit. The neutral condition is studied in many works since wind and temperature field patterns are much easier to capture than the thermally unstable and stable conditions. The other thermal stability conditions have received less attention in the literature. A realistic kidney-shape mine is used in this study, and both a shallow (100 m) and a deep (500 m) mine are considered. The CFD model is used to simulate conditions where the ambient (upwind) flow is thermally unstable, neutral, or stable. An important step in the model evaluation is the comparison of the modeled flow variables upwind to field data collected upwind of an actual open-pit mine.

1.2. Organization of article

In the present study, first the details of the CFD model are presented with governing equations in section 2.1. Then the methodology to quantify the friction velocity and Obukhov length in the CFD model is presented in section 2.2. Next, the field observation campaign and the instruments deployed are introduced in section 2.3. The observation datasets have been used for evaluation of the model. In section 3, the result of the simulations for the two types of open-pit mines (shallow and deep) under thermally unstable, neutral, and stable conditions are presented. Section 4 includes the main conclusions and recommendations.

2. Methodology

2.1. Computational Fluid Dynamics model

The VLES method was developed by Aliabadi et al. (2018), and it was tested at wind tunnel scale for its predictions of mean momentum components, temperature, and various turbulence statistics (Aliabadi et al., 2018; Ahmadi-Baloutaki and Aliabadi, 2021). This method is implemented in OpenFOAM 4.1. In this method, turbulence at the inlet is generated with a vortex method (Aliabadi et al., 2018). This method was initially developed by Sergent (2002) and improved by (Xie, 2016). The main idea of the vortex method is generation of velocity fluctuations in the form of synthetic eddies derived from mean statistical information about the flow as a function of space (height above ground) and time. An inlet vortex field eliminated the need of a precursor simulation or implementation of a cyclic boundary condition at inlet-outlet faces. The number of vortices, vortex size, the vorticity, and the vortices life time are controlling parameters in this method (Mathey et al., 2006). The velocity fluctuations are produced by the vortex method on the inlet boundary. The theory is fully developed in the literature (Sergent, 2002; Mathey et al., 2006; Benhamadouche et al., 2006; Xie, 2016) and provides the following velocity fluctuation field for a given time step (Aliabadi et al., 2018)

$$\mathbf{u}(\mathbf{x}) = \frac{1}{2\pi}\sum_{i=1}^{N}\Gamma_i\frac{(\mathbf{x}_i-\mathbf{x})\times\mathbf{m}}{|\mathbf{x}_i-\mathbf{x}|^2}\left(1-e^{-\frac{|\mathbf{x}_i-\mathbf{x}|^2}{2(\sigma_i(\mathbf{x}_i))^2}}\right)e^{-\frac{|\mathbf{x}_i-\mathbf{x}|^2}{2(\sigma_i(\mathbf{x}_i))^2}}, \tag{1}$$

where $\mathbf{u}$ [m s^{-1}] is velocity perturbation at the model inlet that is later superimposed on the mean inlet velocity, $\mathbf{x}$ [m] is position vector on the inlet boundary, N [-] is the number of vortices to be inserted at the inlet, i is the index for the current vortex, Γ_i [m^2 s^{-1}] is the circulation for the current vortex, $\mathbf{x}_i$ [m] is the position vector for the center of the current vortex, $\mathbf{m}$ [-] is unit vector along the stream-wise direction, and $\sigma_i(\mathbf{x}_i)$ [m] is a characteristic length for the radius of current vortex. The velocity fluctuation fields from N [-] vortices are superimposed on the mean velocity field to provide an overall perturbation velocity field at the inlet. In fluid dynamics and turbulence theory, Reynolds decomposition is a mathematical technique used to separate the mean value of a quantity from its fluctuations. For example, for a quantity A, the Reynolds decomposition would be $A = \overline{A} + a$, where $\overline{A}$ denotes the mean value of A and a is the deviation from the mean value due to turbulent fluctuations (Müller, 2006). In this paper, Reynolds decomposition is applied to all variables. A power-law profile is assumed for the mean velocity (Thomas and Williams, 1999) given by

$$\overline{U}(z) = U_{ref}\left(\frac{z}{z_{ref}}\right)^{\alpha}, \tag{2}$$

where z_{ref} [m] is a reference height, U_{ref} [m s^{-1}] is a reference velocity, and α [-] is an exponent parameterized as a function of aerodynamic roughness length. The relationship between exponent α [-] and the characteristic aerodynamic roughness length of the surface z_0 [m] and turbulence intensity profile are given as (Aliabadi et al., 2018)

$$\alpha = \frac{1}{\ln\left(\frac{z_{ref}}{z_0}\right)}, \tag{3}$$

$$I_u(z) = \frac{1}{\ln\left(\frac{z}{z_0}\right)}. \tag{4}$$

In atmospheric flows there is a limit to $I_u(z)$ [-] of typically the order of unity (Stull, 1988; Nozawa and Tamura, 2002; Aliabadi et al., 2018). The parameterization of sub-grid turbulence kinetic energy (k_{sgs} [m^2 s^{-2}]) is

$$k_{sgs}(z) = 1.5\left[\overline{U}(z)I_u(z)\right]^2. \tag{5}$$

The characteristic size of the inlet vortices can be approximated by the scale of the inlet boundary given by $L_{\text{in}} = \frac{2L_zL_y}{L_z+L_y}$ [m] for the energy-containing eddies. L_z [m] and L_y [m] are inlet height and width. The size of the largest energy-containing vortices, i.e. σ_{max} [m], scales with L_{in} [m] as for atmospheric boundary-layer flow simulations the boundary-layer height δ [m] is in the order of L_{in} [m] for economized models. The relation between σ_{max} [m] and L_{in} [m] is established using a constant a_σ [-], to be defined later, as

$$\sigma_{max} = a_\sigma L_{\text{in}}. \tag{6}$$

The condition of $\Delta < \sigma_{max}$ (Xie, 2016) for the grid spacing Δ [m] should be satisfied in the coarsest region of mesh in a VLES simulation. This condition enables the VLES to resolve the transport, dynamics, and breakdown of the largest eddies in the flow. The size of energy-containing vortices or eddies is a function of height and must decrease with decreasing height. Energy-containing vortex size is parameterized using the mixing length approach of Mellor and Yamada (1974) such that

$$\frac{1}{\sigma(z)} = \frac{1}{\sigma_{max}} + \frac{1}{\kappa(z+z_0)}, \tag{7}$$

where, $\kappa = 0.4$ [-] is the von Kármán constant. This formulation implies that $\sigma(z) \to \kappa z_0$ as $z \to 0$ and $\sigma(z) \to \sigma_{max}$ as $z \to \infty$. In the synthetic vortex method, $\sigma(z) = \sigma(\mathbf{x})$, so the energy-containing eddy size is represented at each height above ground, and it is incumbent upon the simulation to create the energy cascade, down to the local grid size Δ [m], within a short adaptation distance downstream of the inlet.

A characteristic time for the largest energy-containing vortices or eddies can be approximated using scaling. For the largest energy-containing eddies, the characteristic velocity U_0 [m s^{-1}] can be defined using the power-law and the reference height $U_0 = az_{ref}^{\alpha}$. For such eddies the length-scale can be found using $\ell_0 = \sigma_{max}$ [m]. The Reynolds number of the largest energy-containing eddies can be calculated with these two scales as $Re_{\ell_0} = U_0\ell_0/\nu$ [-]. These provide estimates for the Kolmogorov length-scale $\eta = \ell_0 Re_{\ell_0}^{-3/4}$ [m], Kolmogorov velocity scale $u_\eta = U_0 Re_{\ell_0}^{-1/4}$ [m s^{-1}], and dissipation rate $\varepsilon = \nu(u_\eta/\eta)^2$ [m^2 s^{-3}]. The characteristic life time for the largest energy-containing eddies in the flow can be given as (Aliabadi et al., 2018)

$$\tau_0(\ell_0) = \left(\frac{\ell_0^2}{\varepsilon}\right)^{1/3}. \tag{8}$$

This time scale is representative of only the largest eddies. Defining a representative time scale for all energy-containing eddies is possible by assuming a constant a_τ [-], to be adjusted later, given by

$$\tau = a_\tau\tau_0(\ell_0). \tag{9}$$

At the inlet, a new set of vortices can be sampled after every fixed number of iterations by use of this time scale. An incompressible turbulent flow based on a one-equation SGS model is considered. The dimensionless Navier-Stokes equations are developed and discussed below using a reference length-scale such as the boundary-layer height δ [m], a reference upstream velocity U_0 [m s^{-1}], a reference temperature Θ_0 [K], and a reference passive scalar S_0 [-]. With this model, the transport equations become

$$\frac{\partial\overline{U}_i}{\partial x_i} = 0, \tag{10}$$

$$\frac{\partial\overline{U}_i}{\partial t} + \frac{\partial}{\partial x_j}\overline{U}_i\overline{U}_j = -\frac{\partial\overline{P}}{\partial x_i} - \frac{\partial\tau_{ij}}{\partial x_j} + \frac{1}{Re}\frac{\partial^2\overline{U}_i}{\partial x_j\partial x_j} + Ri\delta_{i3}, \tag{11}$$

$$\frac{\partial \overline{\Theta}}{\partial t}+\frac{\partial}{\partial x_i}\overline{U}_i\overline{\Theta}=-\frac{\partial \pi_i}{\partial x_i}+\frac{1}{RePr}\frac{\partial^2\overline{\Theta}}{\partial x_i\partial x_i}, \tag{12}$$

$$\frac{\partial \overline{S}}{\partial t}+\frac{\partial}{\partial x_i}\overline{U}_i\overline{S}=-\frac{\partial \sigma_i}{\partial x_i}+\frac{1}{ReSc}\frac{\partial^2\overline{S}}{\partial x_i\partial x_i}, \tag{13}$$

$$\frac{\partial k_{sgs}}{\partial t}+\overline{U}_i\frac{\partial k_{sgs}}{\partial x_i}=P+B-\varepsilon+\frac{\partial}{\partial x_i}\left(\frac{2}{Re_T}\frac{\partial k_{sgs}}{\partial x_i}\right) \tag{14}$$

Even though all terms in these equations are explained in detail in other works (Li et al., 2010; Aliabadi et al., 2017; Ahmadi-Baloutaki and Aliabadi, 2021), all the terms are described briefly here after transforming them from dimensionless to dimensional quantities. The over bar notation indicates the spatially-resolved solution for a variable. $\overline{P}=\overline{P}_*+\frac{1}{3}\tau_{ii}$ [m^2s^{-2}] is the resolved-scale modified kinematic pressure, which is normalized by constant density, where $\overline{P}_*$ [m^2s^{-2}] is the resolved-scale static kinematic pressure. k_{sgs}[m^2s^{-2}] is SGS TKE. $\tau_{ij}=\overline{U_iU_j}-\overline{U}_i\overline{U}_j=-2\nu_T\overline{S}_{ij}$ [m^2s^{-2}] is the SGS momentum flux, where $\overline{S}_{ij}=\left(\frac{\partial\overline{U}_i}{\partial x_j}+\frac{\partial\overline{U}_j}{\partial x_i}\right)$ [s^{-1}] is the rate of strain and $\nu_T=C_k k_{sgs}^{1/2}l$ [m^2s^{-1}] is turbulent viscosity, in which C_k [-] is a constant and l [m] is the SGS mixing length to be defined later. $\pi_i=\overline{U_i\Theta}-\overline{U}_i\overline{\Theta}=\frac{-\nu_T}{Pr_T}\frac{\partial\overline{\Theta}}{\partial x_i}$ [m s^{-1} K] is the SGS kinematic heat flux, where $Pr_T=0.85$ [-] is the turbulent Prandtl number. In the logarithmic region, Pr_T is expected to be a constant for fluids with molecular Prandtl numbers of order unity, such as air and water (Reynolds, 1975; Li et al., 2015). In this region, Pr_T should be independent of the distances from the wall and can be inferred from the slopes of the normalized mean velocity and temperature profiles (Kays, 1994). It is known, both theoretically and experimentally, that turbulent transport of heat in the ABL, relative to turbulent transport of momentum, is enhanced under thermally unstable conditions due to the role of buoyancy. From the extensive laboratory experiments, field experiments, and theoretical work, one expects that the value of Pr_T should range from 0.7 to 0.9 (Li, 2019). $\mathrm{Re}=\frac{U_0\delta}{\nu}$ [-] is the Reynolds number, $Re_T=\frac{U_0\delta}{\nu_T}$ [-] is the SGS model turbulence Reynolds number, $Pr=\frac{\nu}{\alpha}$ [-] is the laminar Prandtl number, in which α[m^2s^{-1}] is molecular thermal diffusivity. $Ri=\frac{g\delta\Delta\Theta}{\Theta U_0^2}$ [-] is the bulk Richardson number. The SGS component of the passive scalar transport is modeled using the eddy-viscosity assumption, $\sigma_i=\overline{U_iS}-\overline{U}_i\overline{S}=\frac{-\nu_T}{Sc_T}\frac{\partial\overline{S}}{\partial x_i}$ [m s^{-1}], where $Sc_T=0.85$ [-] is the turbulent Schmidt number. The turbulent Schmidt number Sc_T is a non-dimensional variable, describing the ratio of the turbulent transfer of momentum over the turbulent transfer of atmospheric species (Koeltzsch, 2000). The suggested range of Schmidt number for ABL studies is from 0.5 to 1 (Yakhot et al., 1987; Flesch et al., 2002; Gualtieri et al., 2017), with 0.8 being a typical value justified by wind tunnel testing and numerical simulations (Yuan et al., 2017). $P=-\tau_{ij}\overline{S}_{ij}$ [m^2 s^{-3}] is the shear production. $B=-\frac{g\nu_\theta}{\overline{\Theta}}\frac{\partial\overline{\Theta}}{\partial z}$ [m^2 s^{-3}] is the buoyant production. $\varepsilon=\frac{C_\varepsilon k_{sgs}^{3/2}}{l}$ [m^2 s^{-3}] is the dissipation rate. δ_{ij} [-] is the Kronecker-delta function. By using parametrizations for the remaining quantities, the turbulence model is closed. C_k [-] is taken to be 0.094, and C_ε [-] is taken to be 1.048. The length-scale is estimated as a function of local grid size but damped near the walls using van Driest damping functions to prevent excessive dissipation of TKE near the walls (Van Driest, 1956). The length-scale, not near the walls where damping functions are used, is formulated as

$$l=C_\Delta(\Delta x\Delta y\Delta z)^{1/3}, \tag{15}$$

where C_Δ [-] is a parameter to control l [m] and therefore the SGS model. This SGS model is known as `oneEqnEddy` in OpenFOAM.

The inflow is along the x axis, the y axis is in the span-wise direction, and the z axis is vertical direction above ground. For velocity, the synthetic vortex method is used at the inlet, the no-slip condition is used at the domain bottom, slip condition is used on the domain top, and the zero-gradient condition is used at the outlet. The `mappedField` boundary condition, which is a tool in OpenFOAM to map the desired values to each grid cells, is used to set the potential temperature profile at the inlet. This boundary condition provides a self-contained version of the mapped condition. It does not use information on the patch; instead it holds the data locally (Greenshields, 2016). A spatially-uniform fixed value is used for potential temperature on the bottom surface, and zero gradient condition is used on the top and outlet surfaces. The `mappedField` boundary condition is also used to set a fixed value of 1 ppm for the passive scalar at the bottom of the domain on the footprint of the mines. Zero gradient condition is used on the top and outlet surfaces. Airflow enters the domain from the west side, and the outlet of the domain is on the east side. The cyclic boundary condition is assumed for the north and south boundaries for all variables. For the cyclic boundaries, two mapped boundaries are needed for both sides. To make the boundary condition meet this criterion, at the north and south, the domain is expanded from the sides to form two mapped vertical planes.

For SGS TKE, the `atmBoundaryLayerInletK` boundary condition, which assumes that the entire inlet boundary is in the inertial surface layer of ABL, is used at inlet (Stull, 1988). The friction velocity in this boundary condition is calculated by assuming the log-law, as

$$u_*=\frac{\kappa U_{ref}}{\ln\left(\frac{z_{ref}+z_0}{z_0}\right)}, \tag{16}$$

which then computes a uniform SGS TKE as $k_{sgs}=u_*^2/C_\mu^{1/2}$ [m^2 s^{-2}], where $C_\mu=0.09$ [-] is a constant. Much of the TKE is contained in the scales resolved by VLES, so it is expected that k_{sgs} [m^2 s^{-2}] will sharply drop in the stream-wise direction near the inlet, but it will stabilize in the interior of the domain in the stream-wise direction. Specification of k_{sgs} [m^2 s^{-2}] in this manner will provide a convenient method to develop the inlet condition for the synthetic vortex method. The zero-gradient condition is used at the outlet as well as the inlet and outlet for the turbulent viscosity.

At the bottom surface (wall) the `nutkAtmRoughWallFunction` boundary condition is used. This condition modifies the turbulent viscosity near the surface such that

$$\nu_T=\nu\left(\frac{\kappa z^+}{\ln \overline{E}}-1\right), \tag{17}$$

where, $z^+=u_*z/\nu$ [-] is the non-dimensional wall-normal distance, and $\overline{E}=(z+z_0)/z_0$ [-]. Based on the environmental flow wall function, the chosen wall function for the model is given by (Raupach et al., 1991)

$$U^+=\frac{1}{\kappa}\ln\left(\frac{z+z_0}{z_0}\right)\approx\frac{1}{\kappa}\ln\left(\frac{z}{z_0}\right), \tag{18}$$

where z_0 [m] is characteristic aerodynamic roughness length of the surface, $\kappa=0.4$ [-] is the von Kármán constant, and U^+ [-] is non-dimensional mean horizontal velocity. For TKE, the following wall function, which is known as `kqRWallFunction` in OpenFOAM, is used (Greenshields, 2016)

$$k_{sgs}=\frac{u_\tau^2}{C_\mu^{1/2}}, \tag{19}$$

where $C_\mu=0.09$ [-] is a constant. The wall function for temperature used in the current VLES method is inspired from Aliabadi (2018) that correlates the $\Theta^+=(\Theta_s-\Theta)\rho c_p u_\tau/q_s$ [-] (where q_s is surface heat flux) and the logarithm of z^+ [-] via a linear relationship as

$$\Theta^+=\frac{1}{\kappa_\theta}\ln(z^+)+B_\theta, \tag{20}$$

where $\kappa_\theta = 0.48$ [-] is the thermal von Kármán constant, and $B_\theta = 3.9$ [-] is a turbulence model constant. However, it is more common to formulate the Θ^+ [-] based on the U^+ [-] as

$$\Theta^+ = Pr_T\left(U^+ + Pr_f\right), \tag{21}$$

where Pr_T [-] is the turbulent Prandtl number, and Pr_f [-] is described by Jayatillaka (1969). This wall function is known as `alphatJayatillekeWallFunction` in OpenFOAM. In the VLES method, turbulent Prandtl number near the wall can be different from the turbulent Prandtl number in the interior of the domain. Considering the proposed range of 0.3–1 in the literature (Yakhot et al., 1987; Kays, 1994; Li et al., 2015; Li, 2019)) a turbulent Prandtl number of $Pr_T = 0.3$ [-] is chosen for the wall treatment in the simulations.

2.2. Calculation of the CFD model friction velocity and obukhov length at the reference height

According to Monin-Obukhov Similarity Therory (MOST) (Monin and Obukhov, 1954), the vertical profiles of wind and temperature in the thermally neutral atmospheric surface layer follow a logarithmic form, which reduces to zero wind or a fixed surface temperature at ground level. However, when thermal stability is taken into account, the profile can deviate significantly from the standard thermally neutral logarithmic profile (van der Laan et al., 2017; Moradi et al., 2021). In MOST, L [m] denotes the Monin-Obukhov length, which defines atmospheric thermal stability, defined as

$$L = -\frac{\overline{\Theta}_{10\mathrm{m}} u_*^3}{\kappa g \overline{w\theta}}, \tag{22}$$

where u_* [m s^{-1}] is the friction velocity, $\overline{\Theta}_{10\mathrm{m}}$ [K] is the potential temperature at a reference height, $\kappa = 0.4$ [-] is the von Kármán constant, and $\overline{w\theta}$ [m s^{-1} K] is the turbulent sensible kinematic vertical heat flux.

To compare to observed reference friction velocity and Obukhov length, the values of friction velocity and Obukhov length from the CFD model are calculated. The CFD model computes the resolved (k_{res}) and SGS (k_{sgs}) components of TKE [m^2 s^{-2}] as well as the resolved vertical sensible kinematic turbulent heat flux ($\overline{w\theta}_{res}$ [m s^{-1} K]). These values are used, combined with scaling formulations of Panofsky et al. (1977), to estimate the total friction velocity and Obukhov length from the model. The friction velocity is related to the total TKE via

$$k_{tot} = k_{res} + k_{sgs} = \frac{u_*^2}{2}\left(\frac{\overline{u^2}}{u_*^2} + \frac{\overline{v^2}}{u_*^2} + \frac{\overline{w^2}}{u_*^2}\right) \tag{23}$$

Scaling of terms in the bracket enable calculation of the friction velocity as a function of k_{tot} by rearranging this equation. For thermally stable and neutral conditions, the terms in the bracket are scaled as

$$\frac{\overline{u^2}}{u_*^2} = b_u^2, \frac{\overline{v^2}}{u_*^2} = b_v^2, \frac{\overline{w^2}}{u_*^2} = b_w^2, \tag{24}$$

where $b_{u,v,w}$ [-] is 2.5, 2.0, and 1.25, respectively. For the thermally unstable conditions, the vertical component of Eq. (23) is scaled using

$$\frac{\overline{w^2}}{u_*^2} = b_w^2\left(1 - 3\frac{z}{h}\right)^{2/3}, \tag{25}$$

where $z = 10$ m is the reference height and $h = 1000$ m is an assumed length scale representing the height of the planetary boundary layer. Further, the horizontal components of Eq. (23) can be scaled using

$$\frac{\overline{u^2}}{u_*^2} = b_u^2 + \frac{0.35 w_*^2}{u_*^2}, \tag{26}$$

$$\frac{\overline{v^2}}{u_*^2} = b_v^2 + \frac{0.35 w_*^2}{u_*^2}, \tag{27}$$

where $w_{*,res}$ [m s^{-1}] is the convective velocity scale (also known as the Deardorff velocity) calculated using h [m], $\overline{w\theta}_{res}$ [m s^{-1} K], and $\overline{\Theta}_{10\mathrm{m}}$ [K] (the reference potential temperature) as

$$w_{*,res} = \left(\frac{h g \overline{w\theta}_{res}}{\overline{\Theta}_{10\mathrm{m}}}\right)^{1/3}, \tag{28}$$

where g [m s^{-2}] is gravitational acceleration. The non-linearity of the equations above under the thermally unstable condition requires an iterative solution for u_*. To calculate the Obukhov length, only the resolved vertical sensible kinematic turbulent heat flux ($\overline{w\theta}_{res}$ [m s^{-1} K]) is available. Therefore, only the resolved friction velocity (u_{*res} [m s^{-1}]) will be used in the L [m] calculation:

$$L_{res} = -\frac{\overline{\Theta}_{10\mathrm{m}} u_{*,res}^3}{\kappa g \overline{w\theta}_{res}}. \tag{29}$$

2.3. Field observations

The field observation measurements were performed in an open-pit mining facility in northern Canada in May 2018 and July 2019. The field was located near the Wood Buffalo National Park of Canada. Open-pit mining excavations were primarily conducted over the mine area. The mine was approximately 100-m deep with a width and length of 1500 m and 2000 m, respectively. A sonic detection and ranging (sodar) device, a Tethered Air Blimp (TAB) (Byerlay et al., 2020; Nambiar et al., 2020a), and an ultrasonic anemometer were used to determine profiles of wind speed and potential temperature as well as friction velocity and turbulent sensible heat flux at a reference height of $z = 10$ m.

Wind speed and direction were measured with a 4000 series mini sodar instrument by Radiometrics Corporation[1] with a vertical resolution of 10 m from 30 m to 200 m altitudes with an output frequency of 60 min. This acoustic wind profiler had the capacity of measuring wind speed from 0 to 50 m s^{-1} with an accuracy of ±0.5 m s^{-1} and wind direction from 0 to 359° with an accuracy of ±5°.

The customized Tethered Air Blimp (TAB) contained a micro-climate sensor called TriSonica™ Mini weather station by Applied Technologies, Inc.[2] to measure wind speed, wind direction, pressure, temperature, and relative humidity with a sampling frequency of 10 Hz (Byerlay et al., 2020; Nambiar et al., 2020a). It was capable of measuring temperature from 248.15 to 353.15 K, wind speed from 0 to 30 m s^{-1}, pressure from 50 to 115 kPa, and relative humidity from 0 to 100%. The measurement resolution of this mini weather station was ±0.1 m s^{-1} for wind speed, ±1° for wind direction, and ±0.1 K for temperature. Moreover, the accuracy of measurement for wind speed was ±0.1 m s^{-1}, for wind direction was ±1°, and for temperature was ±2 K. The TAB was launched up to an altitude of 200 m from the surface. Meteorological variables were statistically sampled every 5 min to produce means of horizontal wind speed and potential temperature as a function of time of day and height.

A CSAT 3B ultrasonic anemometer measured the three-dimensional wind components and temperature at a sampling frequency of 10 Hz as recommended by Aliabadi et al. (2019) from Campbell Scientific Inc.[3] which is used to calculate the turbulent statistics u_* [m s^{-1}] and L [m]. The anemometer had the capability of measuring wind speeds up to 30 m s^{-1} and temperature from 243.15 to 323.15 K. The measurement resolutions of the ultrasonic anemometer was ±0.001 m s^{-1} for

[1] http://radiometrics.com.
[2] http://www.apptech.com.
[3] https://www.campbellsci.ca.

horizontal wind, ±0.0005 m s^{-1} for vertical wind, ±0.058° for wind direction, and ±0.002 K for temperature. Moreover, the accuracy was ±0.08 m s^{-1} for horizontal wind, ±0.04 m s^{-1} for vertical wind, and ±10° for wind direction.

The ultrasonic anemometer data were used to choose three pairs of friction velocity u_* [m s^{-1}] and Obukhov length L [m] values at the upstream of the domain which represented typical thermal stability conditions associated with unstable, neutral, and stable cases. Next, the selected dates and times were used to retrieve mean horizontal wind speed and potential temperature profile data from the sodar and TAB for comparison to the CFD model results. This procedure provided a consistent approach for model versus observation comparison under the three sets of thermal stability conditions.

2.4. Model geometry and domain size

In the present work, two sets of synthetic mine geometries, namely shallow and deep mines, are simulated to demonstrate the importance of mine depths and wall details in determining flow patterns. Fig. 1 shows the generated shallow and deep mine geometries based on the stepped walls and overall kidney-shape mines. In Table 1 the details of mine wall and dimensions are presented. It can be seen that there are two ramps in the deep mine and one ramp in the shallow mine. Adding more ramps are necessary for the deep mine as the trucks should travel deeper on the wall of the mine. The overall slope and bench face angles are sharper for the deep mine than the shallow mine to make possible digging in the deeper layer. Also, the heights of the benches and ramps are higher for the deep mine than the shallow mine.

The CFD model should simulate the roughness sub-layer in the atmosphere, which is approximately five times the roughness element height (Aliabadi et al., 2017; Moradi et al., 2021). For example, if the domain height is 200 m, the deepest mine that can be simulated is 40 m.

Table 1
Dimensions of the stepped shallow and deep mines.

Geometry	Dimension	
	Shallow Mine	Deep Mine
Overall Slope Angle	30°	50°
Bench Face Angle	60°	70°
Mine Depth	100 m	500 m
Mine Length	1500 m	1500 m
Mine Width	2000 m	2000 m
Bench Height	10 m	25 m
Bench Width	10 m	10 m
Ramp Height	10 m	25 m
Ramp Width	25 m	25 m

To simulate a 500 m deep mine, the domain height should be 2500 m. Since a 500-m deep mine is investigated, the height of the domain is 2500 m for all simulations. For both cases, the domain length and width are 10000 m and 6000 m, respectively. The mines' upstream edge is located after the half point in the stream-wise direction. This allows for an adaptation distance such that flow mean and turbulence statistics adopt representative atmospheric conditions before studying transport phenomena over the mines.

2.5. Numerical schemes, solution control, averaging, and probing

A second-order implicit backward time scheme is used. Gradient schemes are based on second-order Gaussian integration with linear interpolation. All Laplacian schemes are based on corrected Gaussian integration with linear interpolation, which provide unbounded, second-order, and conservative numerical behavior. Divergence schemes are based on Gaussian integration with linear or upwind interpolation, depending on the variable of interest (Greenshields,

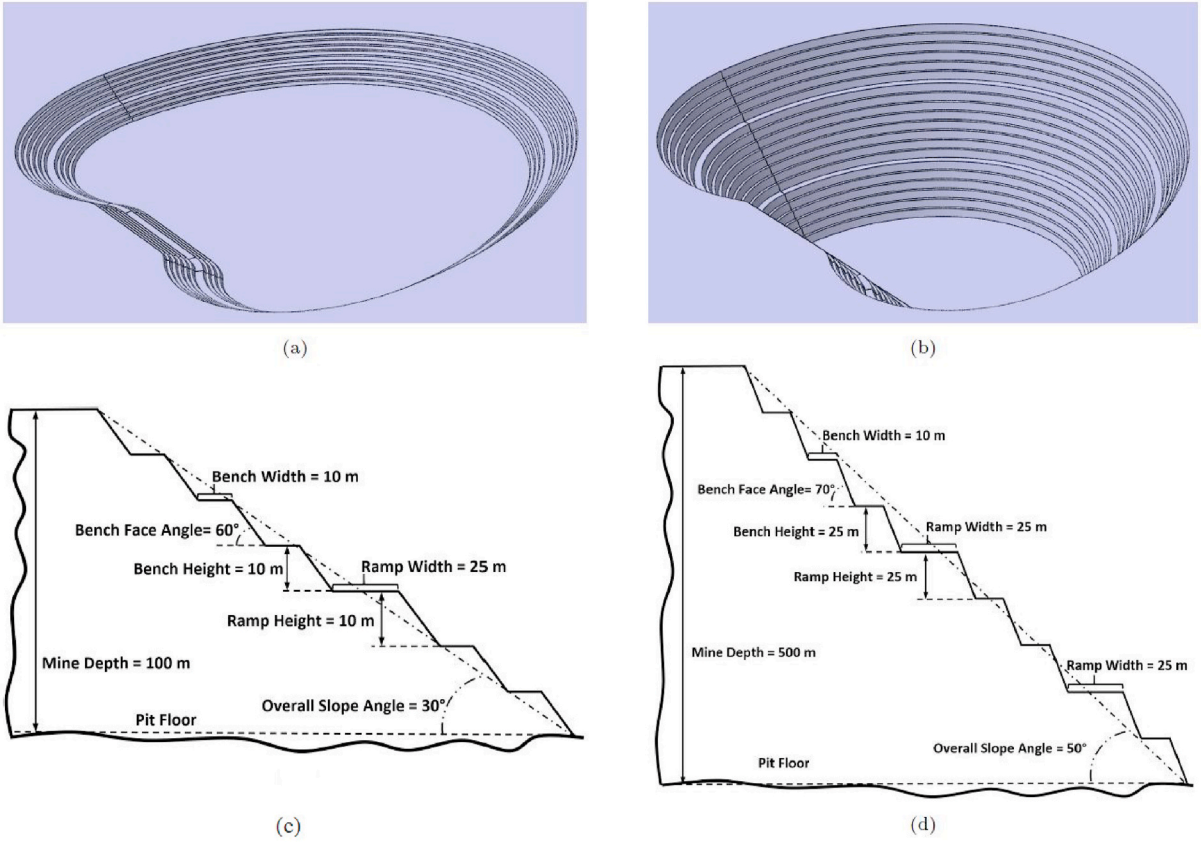

Fig. 1. a) Shallow and b) deep synthetic mine geometries, c) shallow and d) deep synthetic mine walls.

2016).

Throughout all simulations, time-steps are chosen so that the maximum Courant number satisfies $Co = \Delta t\left|\overline{U}\right|/\Delta x < 0.1$ [-]. The pressure matrix is preconditioned by the diagonal incomplete Cholesky technique and solved by the preconditioned conjugate gradient solver. Other variables are preconditioned by the diagonal incomplete-lower-upper technique and solved by the preconditioned bi-conjugate gradient solver. The pressure-linked equations (i.e. equations that have a pressure term) are solved by a hybrid method consisting of two algorithms: 1) the pressure-implicit split-operator method and 2) the semi-implicit method (Greenshields, 2016).

In Table 2 the important input variables of the VLES method are presented. The potential temperature difference (top minus bottom) at the inlet for the thermally unstable and stable conditions are set to − 2 K and +5 K, respectively. This potential temperature difference is set between the surface up to 100 m, and after that, the potential temperature is constant to the top of the domain. The filter size parameter (C_Δ) [-] is chosen to be higher for thermally unstable conditions than the thermally neutral and stable conditions. A smaller C_Δ [-] causes less turbulence fluctuation near the surfaces, where turbulence is mostly modeled. In the thermally stable conditions, the atmosphere is calmer than the thermally unstable conditions and a smaller C_Δ [-] helps the model to represent the thermally stable condition better. The length-scale and time-scale constants (a_σ [-] and a_τ [-]) are set to 1 and these constants remained fixed for all thermal stability conditions. As the Turbulence Intensity (TI) decreases with increasing thermal stability, less turbulence is injected in the domain. The TI tends to be higher in thermally unstable conditions, than in the thermally stable conditions (Hansen et al., 2012; Aliabadi et al., 2017). In the present simulations, higher TI is chosen for the thermally unstable conditions (TI = 0.3 [-]) than the thermally neutral or stable conditions (TI = 0.1 [-]). Surface roughness is $z_0 = 0.3$ m all over the domain, which creates a uniform aerodynamic roughness for all surfaces (Raupach et al., 1991). To create the desired power-law velocity profile, two parameters (U_{ref} [m s^{-1}] and z_{ref} [m]) are used to define the inlet wind profile. It should be noted that the combination of U_{ref} and z_{ref} affect the velocity profile at the inlet.

After the flow passes over the domain in the stream-wise direction once with a time step of 0.1 s, the simulations are extended for an additional two flow passes over the domain with a time step of 0.01 s to obtain statistical information by time averaging. Note that with a finer time step of 0.01 s, the solution is extracted at a sampling rate of 0.1 s to match the ultrasonic anemometer sampling frequency (10 Hz). Note that one pass can be interpreted as the characteristic flow time in the stream-wise direction, and multiple characteristic flow times must be reached before obtaining statistical information about the flow. The smaller time step in Table 2 helps extracting more accurate averages for comparison to observations. The averaging period is set to 15 min.

To statistically sample the flow characteristics in order to compare the model results with field measurements, two sets of probes are inserted inside the domain. To analyze the upstream and downstream surface-layer profiles, the first set of probes are used. These are distributed on 10 profiles (P1 to P10), which are located in the central axis at $y = 3000$ m to the west and east sides of the mine. Each profile is 100 m tall with 5-m probe spacing in the vertical direction. The second set is additional probes on profiles (P11 to P13) inside the mine that extend up to 100 m altitude above grade. The probe spacing on these is every 5 m. The probing setup can be seen in Fig. 2.

2.6. Grid resolution

The computational grid is generated using the `snappyHexMesh` utility provided in OpenFOAM 4.1. The vertical mesh is refined inside the mine and near the surface to resolve the energy cascade as much as possible close to the ground and inside the mine. The mesh discretization in the vertical direction is set to be 2 m from the bottom of the mine to 100 m above grade (Vertical Region 1 in Table 3); then it increases to 30 m up to 1000 m above ground (Vertical Region 2 in Table 3), and finally, it is set to 75 m up to the top of the domain (Vertical Region 3 in Table 3). The cells are produced with wall-normal dimensions (z^+ [-]) of between 200 and 2000 adjacent to the surface. The z^+ [-] is the distance in wall units between the centroid of the first cell and the wall. Various upper limits have been reported for the z^+ [-] to satisfy the log-law. Conservative estimates suggest $z^+ < 500$–1000 applicable to smooth and very rough walls with intercept adjustments (Blocken et al., 2007). Non-conservative upper limits have been shown to exhibit a near log-law behaviour for $z^+ \rightarrow 10000$ [-] (Kays and Crawford, 1993). However, it is impossible to satisfy this criterion everywhere when processes of flow separation and attachment occur. The mesh in the horizontal direction is divided into two sections. First, a very fine mesh is generated surrounding the mine area from $x = 2500$ m to 9000 m that extends to the edges of the domain with a grid spacing of 50 m by 50 m (Horizontal Region 1 in Table 3). Second, a coarse mesh is used near the inlet ($x = 0$ m to 2500 m) and outlet ($x = 9000$ m to 10000 m) of the domain, with a grid spacing of 170 m by 170 m (Horizontal Region 2 in Table 3). This kind of mesh is generated to simulate the flow more accurately in the sensitive areas, which is close to the center of the domain and, in the meantime, to avoid high computational cost elsewhere. A sensitivity analysis on the mesh is performed to select the best cell number for each mine type. Four different numbers of mesh elements in horizontal and vertical directions (Table 3) are generated for the shallow mine under the thermally unstable case. For each case, the velocity and potential temperature profiles on P3 (Fig. 2) are plotted and compared with the observations of TAB (Fig. 3). By looking at Fig. 3, it is evident that the profiles associated with 0.5M and 1M cells deviate from the profiles of the observation, while results associated with 1.6M and 2M simulations are closer to the observations.

Table 4 shows the Bias= $\frac{\sum_{i=1}^{n}(M_i - O_i)}{n}$ and Root Mean Square Error (RMSE)= $\sqrt{\frac{\sum_{i=1}^{n}(M_i - O_i)^2}{n}}$ of mean horizontal velocity and potential temperature profiles predicted by CFD (M_i) in comparison to observed TAB data (O_i). The Bias and RMSE of the cases with 1.6M and 2M mesh elements are lower than other cases. It is confirmed that the selected mesh resolution with 1.6M cells provides better accuracy than the lower resolution simulations, and similar to the 2M cell simulation. Hence, the grid spacing associated with the 1.6M cells is chosen for the rest of the simulations.

Table 2
CFD input variables for different thermal stability and mine depth simulation cases.

Thermal Stability Conditions	Mine Type	C_Δ [-]	a_σ[-]	a_τ [-]	TI [-]	z_0 [m]	U_{ref} [m s^{-1}]	z_{ref} [m]	Time Step 1 [s]	Time Step 2 [s]
Unstable ($\Delta\overline{\Theta} = -2$ K)	Shallow	1	1	1	0.3	0.3	3.5	500	0.1	0.01
	Deep	1	1	1	0.3	0.3	3.5	500	0.1	0.01
Neutral ($\Delta\overline{\Theta} = 0$ K)	Shallow	0.5	1	1	0.1	0.3	10	100	0.1	0.01
	Deep	0.3	1	1	0.1	0.3	10	100	0.1	0.01
Stable ($\Delta\overline{\Theta} = +5$ K)	Shallow	0.001	1	1	0.1	0.3	4	20	0.1	0.01
	Deep	0.001	1	1	0.1	0.3	4	20	0.1	0.01

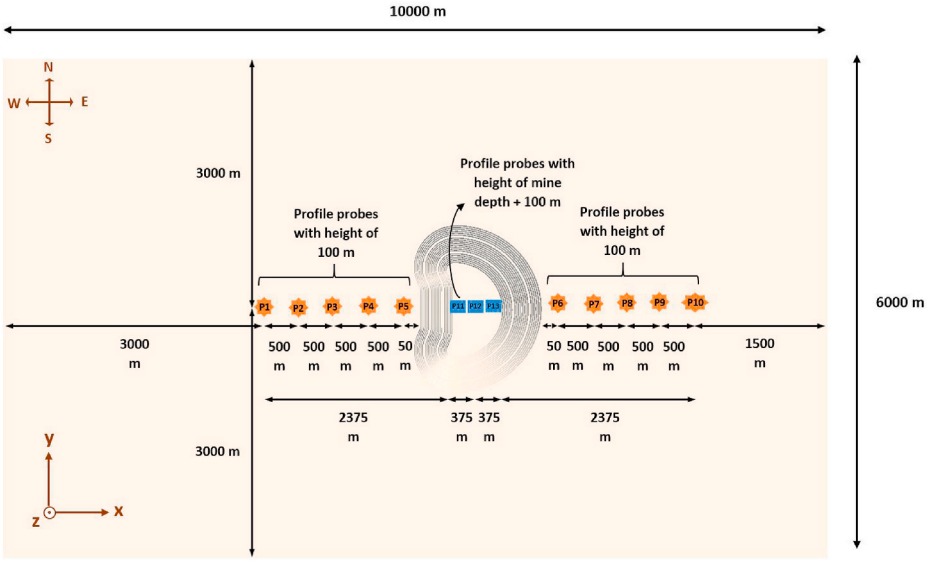

Fig. 2. Top view of probing locations.

Table 3
Different mesh grading options in the horizontal and vertical regions of the simulation domain.

	Horizontal Region 1	Horizontal Region 2	Vertical Region 1	Vertical Region 2	Vertical Region 3
CFD (0.5M cells)	dx = dy = 500 m	dx = dy = 200 m	dz = 20 m	dz = 80 m	dz = 150 m
CFD (1M cells)	dx = dy = 300 m	dx = dy = 100 m	dz = 10 m	dz = 60 m	dz = 100 m
CFD (1.6M cells)	**dx = dy = 170 m**	**dx = dy = 50 m**	**dz = 2 m**	**dz = 30 m**	**dz = 75 m**
CFD (2M cells)	dx = dy = 150 m	dx = dy = 40 m	dz = 1.5 m	dz = 25 m	dz = 60 m

3. Results and discussion

3.1. Comparison against observations

Table 5 shows the values selected for friction velocity u_* and Obukhov length L from the observation to compare the CFD simulations to field observations taken at the actual mine site. The predictions of the CFD model are shown for profile P3 as a representative upstream

Table 4
Bias (RMSE) for mean horizontal velocity ($\overline{U}$) and potential temperature ($\overline{\Theta}$) calculated for CFD on profile P3 with different cell numbers versus observations; data reported for the shallow mine case under thermally unstable condition.

	Bias (RMSE) of $\overline{U}$ [m s^{-1}]	Bias (RMSE) of $\overline{\Theta}$ [K]
CFD (0.5M cells)	−1.09 (1.17)	−0.49 (0.83)
CFD (1M cells)	−1.33 (1.36)	0.28 (0.34)
CFD (1.6M cells)	0.44 (0.84)	−0.19 (0.33)
CFD (2M cells)	0.51 (0.88)	−0.18 (0.30)

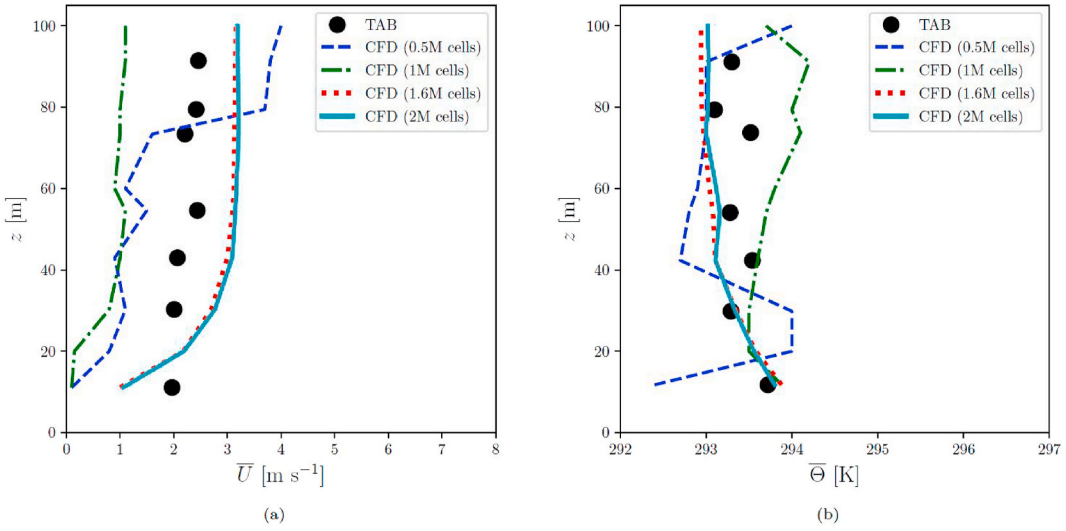

Fig. 3. a) Mean horizontal velocity ($\overline{U}$) and b) potential temperature ($\overline{\Theta}$) profiles at P3 versus observations with different cell numbers for the thermally unstable shallow mine simulation.

Table 5
Friction velocity and Obukhov length: observed and predicted by CFD on profile P3; data reported for shallow and deep mine cases; data reported under various thermal stability conditions.

Mine Type		Observed	CFD (P3)
Thermally unstable			
Shallow	$u_{*,10\ m}$ [m s^{-1}]	0.25	0.29
	$L_{10\ m}$ [m]	−11.00	−11.60
Deep	$u_{*,10\ m}$ [m s^{-1}]	0.25	0.33
	$L_{10\ m}$ [m]	−11.00	−27.18
Thermally neutral			
Shallow	$u_{*,10\ m}$ [m s^{-1}]	0.46	0.46
	$L_{10\ m}$ [m]	–	–
Deep	$u_{*,10\ m}$ [m s^{-1}]	0.46	0.52
	$L_{10\ m}$ [m]	–	–
Thermally stable			
Shallow	$u_{*,10\ m}$ [m s^{-1}]	0.12	0.26
	$L_{10\ m}$ [m]	9.00	9.36
Deep	$u_{*,10\ m}$ [m s^{-1}]	0.12	0.23
	$L_{10\ m}$ [m]	9.00	31.45

location that is far enough from the inlet (for flow to adapt to surface layer characteristics) and far enough from the edge of the mine (for flow not to be influenced by the structure of the flow in the mine). Overall, the agreement between CFD results and the field observations is better for the shallow mine in comparison to the deep mine. The lower level of agreement for the deep mine is due to more complex flow patterns and will be investigated further in the subsequent analysis.

Figs. 4–6 show the upstream vertical profiles of mean horizontal wind speed and potential temperature as measured by the observations and predicted by CFD simulations under the thermally unstable, neutral, and stable conditions, respectively. Note that for the thermally neutral case, the potential temperature is uniform everywhere in the domain, so it is not plotted. Table 6 shows the Bias and RMSE of mean horizontal wind speed and potential temperature calculated for CFD versus observations. It must be noted that both the TAB and sodar instruments sampled the atmosphere over finite times, typically about 30–60 min for each record (Nambiar et al., 2020a). The finite temporal averaging has resulted in some scatter in the observation data for each profile. Therefore, these profiles should be studied for their bulk estimates of potential temperature and wind speed. Obtaining smooth profiles from these measurements would have required analysis of larger datasets for temporal averaging over multiple records meeting the same pair of friction velocity and Obukhov length values. However, due to the limited dataset, this was not possible. Nevertheless, the bulk measures of the atmospheric variables serve as a basis for the evaluation of the CFD model.

For the thermally unstable case (Fig. 4), the agreement between observations and CFD in potential temperature profiles can be examined using Bias (RMSE) for the shallow and deep mines as 0.04 (0.18) and −0.11 (0.17) K, respectively, corresponding to profiles P1 to P3. The agreement in the horizontal wind speed profiles can be reported using

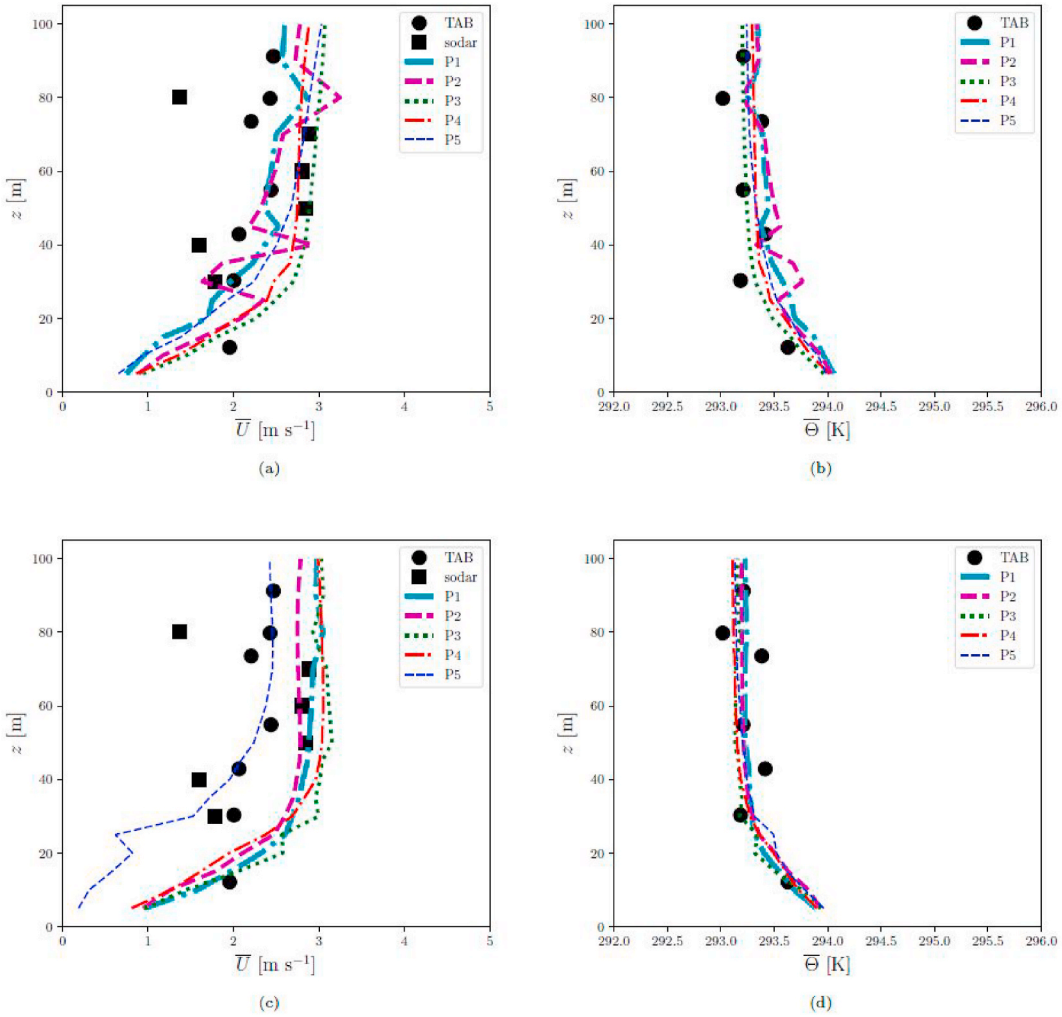

Fig. 4. Mean horizontal wind speed ($\overline{U}$) and potential temperature ($\overline{\Theta}$) profiles predicted by CFD (P1 to P5) and measured using observations (TAB, sodar) for thermally unstable shallow (a and b) and deep (c and d) mine cases.

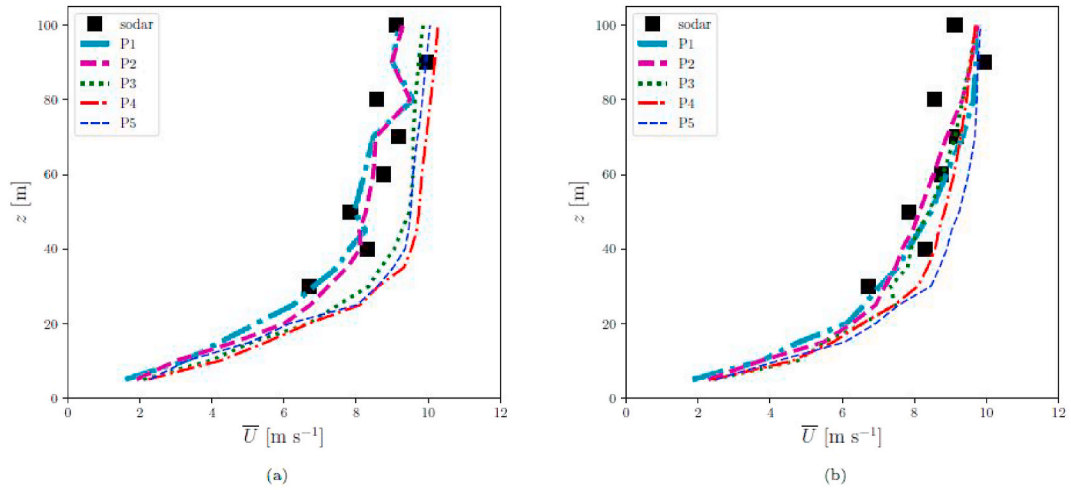

Fig. 5. Mean horizontal wind speed ($\overline{U}$) profiles predicted by CFD (P1 to P5) and measured using observations (sodar) for thermally neutral shallow (a) and deep (b) mine cases.

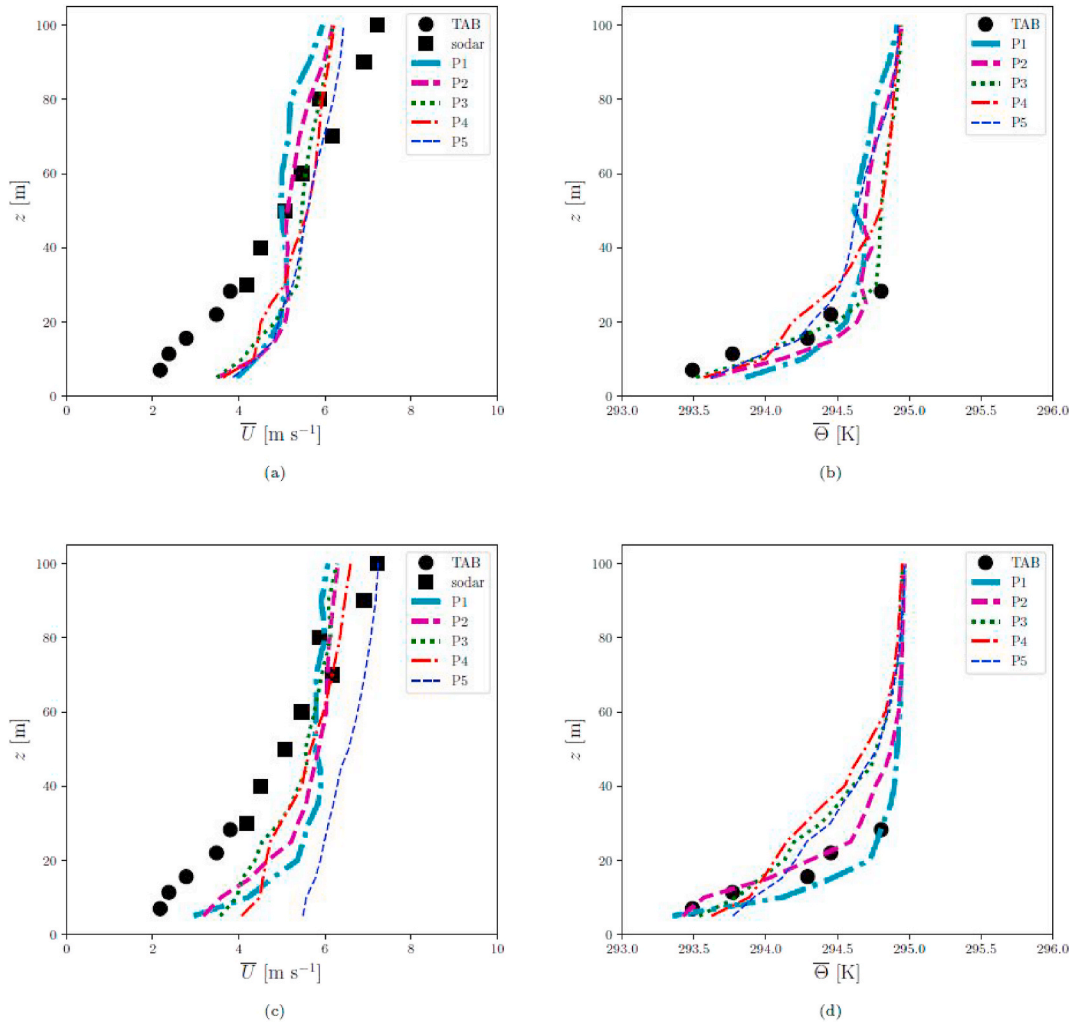

Fig. 6. Mean horizontal wind speed ($\overline{U}$) and potential temperature ($\overline{\Theta}$) profiles predicted by CFD (P1 to P5) and measured using observations (TAB, sodar) for thermally stable shallow (a and b) and deep (c and d) mine cases.

Bias (RMSE) for the shallow and deep mines as 0.35 (0.70) and 0.60 (0.78) m s^{-1}, respectively, by taking the average of error statistics using the TAB and sodar datasets as corresponding to profiles P1 to P3. From the plots, wind speed profile P5 in the deep mine case deviates from the rest of the profiles. Profile P5 is the closest profile to the mine, and it is the most affected by modification of the flow structure in the mine

Table 6
Bias (RMSE) for mean horizontal wind speed ($\overline{U}$) and potential temperature ($\overline{\Theta}$) calculated for CFD versus observations; data reported for shallow and deep mine cases; data reported under various thermal stability conditions.

Mine Type	Ref. data	P1	P2	P3	P_{avg}
Thermally unstable					
Shallow	$\overline{U}$ (TAB) [m s^{-1}]	0.00 (0.42)	0.12 (0.48)	0.41 (0.57)	0.18 (0.49)
	$\overline{U}$ (Sodar) [m s^{-1}]	0.37 (0.79)	0.44 (0.97)	0.79 (1.00)	0.53 (0.92)
	$\overline{\Theta}$ (TAB) [K]	0.08 (0.18)	0.12 (0.22)	−0.08 (0.15)	0.04 (0.18)
Deep	$\overline{U}$ (TAB) [m s^{-1}]	0.45 (0.56)	0.27 (0.45)	0.50 (0.68)	0.41 (0.56)
	$\overline{U}$ (Sodar) [m s^{-1}]	0.80 (1.01)	0.63 (0.89)	0.93 (1.09)	0.79 (1.00)
	$\overline{\Theta}$ (TAB) [K]	−0.11 (0.17)	−0.11 (0.17)	−0.11 (0.17)	−0.11 (0.17)
Thermally neutral					
Shallow	$\overline{U}$ (Sodar) [m s^{-1}]	−0.21 (0.56)	−0.02 (0.53)	0.86 (1.03)	0.21 (0.71)
Deep	$\overline{U}$ (Sodar) [m s^{-1}]	0.25 (0.55)	0.09 (0.52)	0.22 (0.52)	0.19 (0.53)
Thermally stable					
Shallow	$\overline{U}$ (TAB) [m s^{-1}]	1.69 (1.71)	1.77 (1.79)	1.54 (1.56)	1.40 (1.69)
	$\overline{U}$ (Sodar) [m s^{-1}]	−0.41 (0.88)	−0.20 (0.69)	0.00 (0.73)	−0.20 (0.77)
	$\overline{\Theta}$ (TAB) [K]	0.33 (0.44)	0.33 (0.37)	0.18 (0.25)	0.28 (0.35)
Deep	$\overline{U}$ (TAB) [m s^{-1}]	1.69 (1.75)	1.29 (1.30)	1.22 (1.25)	1.40 (1.43)
	$\overline{U}$ (Sodar) [m s^{-1}]	0.25 (0.92)	0.26 (0.78)	0.12 (0.60)	0.21 (0.77)
	$\overline{\Theta}$ (TAB) [K]	0.36 (0.39)	0.04 (0.09)	−0.01 (0.28)	0.13 (0.25)

(mainly circulation of flow). The alteration of the flow structure in the mines will be discussed in subsequent sections in detail. For the thermally neutral case (Fig. 5), the agreement in the horizontal wind speed profiles predicted by CFD versus the observations can be reported using Bias (RMSE) for the shallow and deep mines as 0.21 (0.71) and 0.19 (0.53) m s^{-1}, respectively, corresponding to profiles P1 to P3. It can be seen that the presence of the mines and the alteration of the flow structure in the cavity influences the horizontal wind speed profiles closer to the mines (P3–P5). For the thermally stable case (Fig. 6), the agreement between observations and CFD in potential temperature profiles can be reported using Bias (RMSE) for the shallow and deep mines as 0.28 (0.35) and 0.13 (0.25) K, respectively, corresponding to profiles P1 to P3. The agreement in the CFD wind speed profiles versus the observations can be reported using Bias (RMSE) for the shallow and deep mines as 0.60 (1.23) and 0.80 (1.10) m s^{-1}, respectively, by taking the average of error statistics using the TAB and sodar datasets as corresponding to profiles P1 to P3. It appears that CFD overpredicts wind speed in the lower portion of the surface layer. Similar to the thermally unstable case, in the thermally stable case the horizontal wind speed profile P5 for the deep mine case is affected more significantly by the structure of the flow in the mine compared to the shallow mine case, so it deviates from other profiles.

Focusing on the CFD results, on average, the Biases for wind speed and the potential temperature upstream of the mine are under 0.70 m s^{-1} and 0.2 K, respectively, which imply that the model has the skill to simulate the mean wind speed and potential temperature in the surface layer reasonably well. The thermally unstable cases have the lowest Bias and RMSE compared to the thermally neutral and stable cases. The relative success of LES in simulating convective boundary layers versus thermally stable boundary layers has been noted in previous studies. In thermally stable boundary layers, the buoyancy forces caused by thermal stratification have a stabilizing effect on the boundary layer by suppressing turbulent transport specially in the vertical direction (van der Laan et al., 2017). The damping of turbulent motions by thermal stratification results in generally low turbulence levels along with small-scale eddies populating the boundary layer (Huang and Bou-Zeid, 2013). Most of the successful LES studies of ABL have been conducted on convective boundary layers, which have large energy-containing eddies in the order of the size of the boundary layer height (Gavrilov et al., 2011; Sandham and Waite, 2015; Han et al., 2019). The success of these LES method is mainly attributed to the dominance of the large-scale structures in the convective boundary layer (Sandham and Waite, 2015; Ponomarev et al., 2007). On the other hand, LES of stable boundary layers requires higher grid resolutions and more accurate SGS models to simulate the relatively small boundary-layer turbulence scales reasonably well (Huang and Bou-Zeid, 2013). This requirement may not be satisfied in practical simulations, possibly explaining the lower level of agreement for the thermally stable cases simulated here.

3.2. Spatial variability of fields

Fig. 7 shows the spatial variability of the wind velocity vectors and magnitude contours. The plots are shown for a vertical slice of the domain through the center of the mine ($y = 3000$ m). Skimming flow typically occurs over deep cavities with walls packed close to one another with a small horizontal space between them. Such depressions tend to trap stable vortices and contain pockets of "isolated air". In such cases, the surface tends to act as if it were aerodynamically smooth (Perrier et al., 1972). In the skimming flow regime, the fluid flows down the stepped face of the depression as a coherent stream, and mainly skimming over the steps and cushioned by the recirculating fluid trapped between the faces of the depression. Also, the energy dissipation in the flow appears to be enhanced by the momentum transfer to the recirculating fluid (Rajaratnam, 1990). In the current simulations, the skimming flow over the mine is only predicted under the thermally neutral condition. In this case flow circulations are predicted inside the mine, but they do not influence the flow structure outside the mine significantly. This is in agreement with another CFD study of a deep mine under thermally neutral conditions by Flores et al. (2014) (their Fig. 3a).

Under thermally unstable or stable conditions many complexities in the flow structure are noted by the present simulations. Under the thermally unstable conditions, flow circulations are observed for both the shallow and deep mines although the circulation pattern is more effective for the deep mine. Further the circulation pattern inside the mine influences the flow structure outside the mine, in agreement with CFD study of Flores et al. (2014) (their Fig. 3e). Such flow patterns result from topographical changes in the land, as they were simulated using the Weather Research and Forecasting (WRF) model by Nahian et al. (2020) (their Fig. 7f) in a mine field comparable to the shallow mine in this study. Under thermally stable conditions similar circulations were simulated by Nahian et al. (2020) (their Fig. 7e) and observed in a real earth depression comparable to the deep mine by Clements et al. (2003) (their Fig. 11). Under the thermally stable conditions, the wind speed inside the shallow mine is reduced compared to the surroundings. This is in agreement with simulations of Nahian et al. (2020) (their Fig. 7e). The meteorological conditions of such depressions are understood to be influenced by modified topography, loss of advective momentum transfer with the surrounding atmosphere, and reduced turbulent sensible heat flux at the bottom of the mine (Clements et al., 2003; Whiteman et al., 2004). Under the thermally stable conditions, the wind speed inside the deep mine is enhanced compared to the surroundings due to the formation of a standing wave. This is in agreement with observations in a real earth depression comparable to the deep mine by Lehner et al. (2016) (their Figs. 2 and 10). They observed that the flow across the deep earth depression generates a deep wave in the lee side of

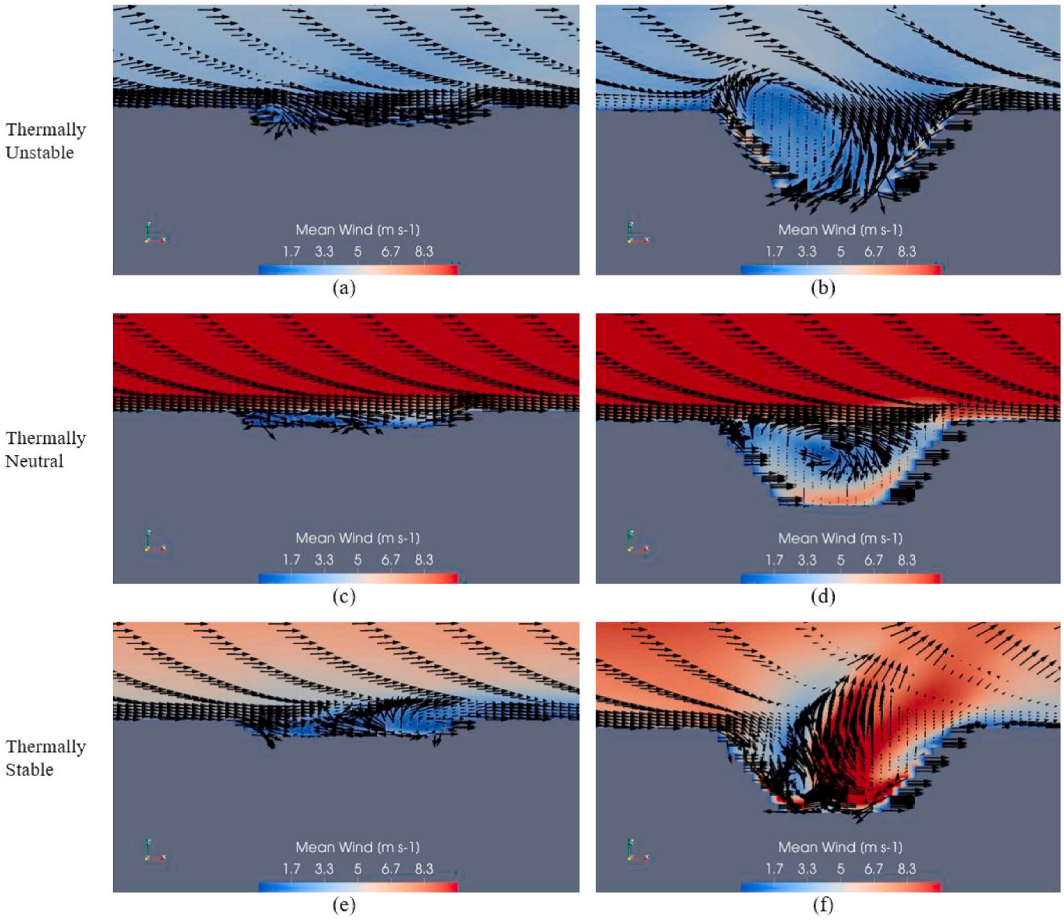

Fig. 7. Wind field velocity vectors and magnitude contours for thermally unstable (a and b), thermally neutral (c and d), and thermally stable (e and f) cases for the shallow (a, c, e) and deep (b, d, f) mines.

the depression, transporting warm air from aloft down into the depression, while typically producing only a small disturbance to the stable air mass in other parts of the depression. This wave further causes a rising structure of air from the bottom of the depression upward into the atmosphere even beyond the surface layer above grade (>200 m).

Fig. 8 shows the spatial variability of the passive scalar field according to thermal stability conditions and mine depth. The dispersion patterns are a direct consequence of flow fields shown in the previous figure. Again, only under the thermally neutral condition, skimming flow is predicted, where the passive scalar circulates inside the mine and then exists downstream as a vertically thin plume confined to elevations below the top of the surface layer (<200 m), which is in agreement with the CFD study of Flores et al. (2014) (their Fig. 7a).

For the thermally unstable case, propagation of the passive scalar upstream and upward is predicted. In the thermally unstable case due to turbulent vertical mixing downstream of the mine, the plume exits the mine as a thick layer reaching altitudes up to and beyond 1000 m within the ABL. In the deep plume at the downwind edge of the mine, due to the large standing vortex in the mine that transports tracer to large heights, the plume rise is more significant for the deep mine than the shallow mine. Simulations of Flores et al. (2014) (their Fig. 7e) reveal similar dispersion patterns, in comparison to the neutral case, where the plume rise in the atmosphere is more significant. Aircraft observations of Gordon et al. (2015) for a real mine representing the shallow mine here also revealed that under thermally unstable conditions, the plume can rise up to a significant portion of the ABL.

For the thermally stable case, the plume dispersion phenomenon is different for the shallow and deep mines. For the shallow mine, a thin vertically shallow plume is predicted downstream of the mine, which is confined within the surface layer, in agreement with WRF simulations of Nambiar et al. (2020b) (their Fig. 7) for a real mine comparable to the shallow mine in this study. However for the deep mine, a vertical rise of the plume is predicted at the center of the mine as a direct consequence of the standing wave. In contrast to the thermally neutral case, this causes a deep plume within a substantial portion of the ABL downstream of the mine.

Fig. 9 shows the horizontal pattern of the passive scalar and velocity fields over a horizontal slice at 10 m above grade (not terrain following). In fact Figs. 7–9 show the complex three dimensionality of the flow field in the present simulations, which reveal the value of CFD simulations in helping understand atmospheric transport. The wind speed at 10 m above grade is much lower under thermally unstable condition than the thermally neutral and stable conditions. Lower wind speeds under unstable conditions are likely due to the presence of a well-mixed convective surface layer, characterized by a near-constant distribution of wind speed with height due to strong vertical mixing (Kaimal et al., 1976). The high wind speed under stable conditions may be due to sharp vertical gradients in the wind speed in the surface layer, which is typically due to suppressed vertical mixing and has been well documented in the literature (Nieuwstadt, 1984; Mahrt and Vickers, 2006). The top view of the wind velocity vectors and passive scalar field show distinct spatial patterns. Horizontal wind circulations inside the mine can be noted under all configurations but are particularly accentuated with the deep mine under the thermally stable case. Such horizontal circulations were also noted by Nahian et al. (2020) for an enclosed earth depression using WRF simulations (their Fig. 7e and f). Under the thermally unstable and neutral cases, large passive scalar values appear as a ring surrounding the mine edge in all directions, possibly due to strong

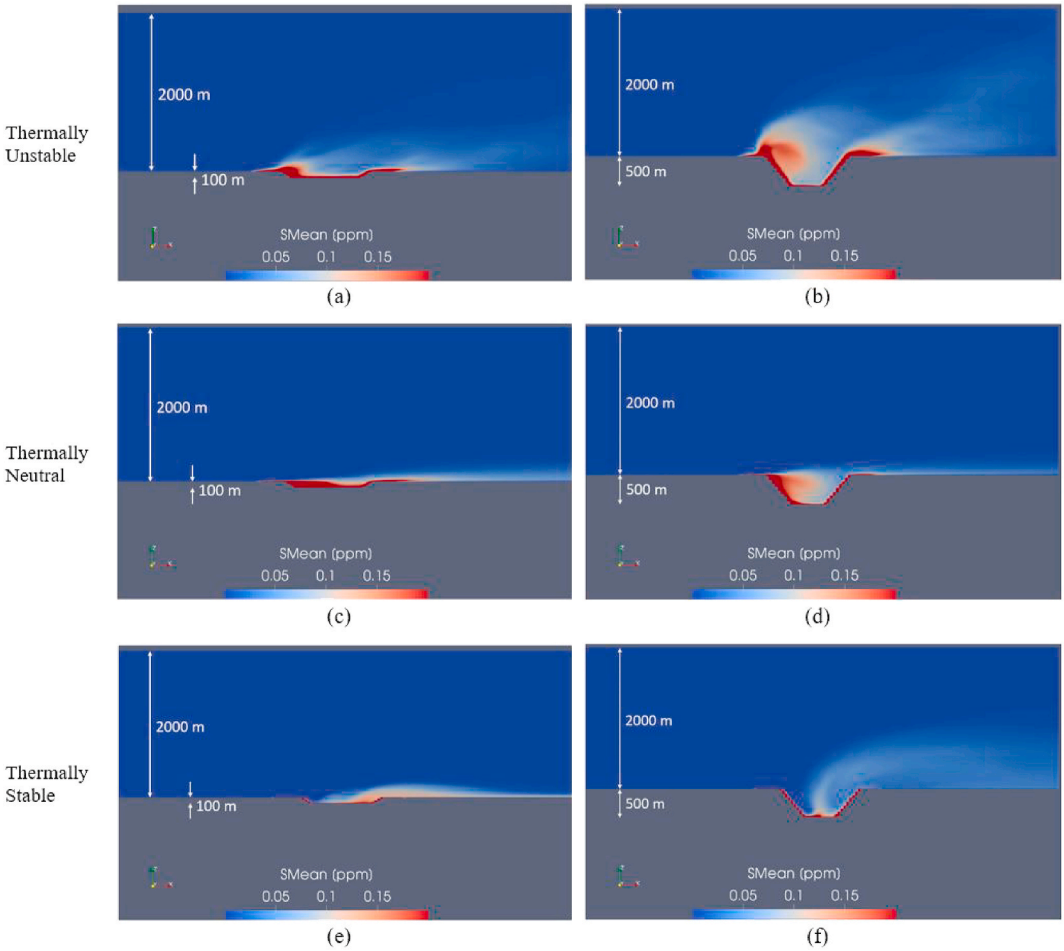

Fig. 8. Passive field contours for thermally unstable (a and b), thermally neutral (c and d), and thermally stable (e and f) cases for the shallow (a, c, e) and deep (b, d, f) mines.

vertical mixing, vertical circulations, and slope flows along the mine walls. However, under the thermally stable case, such rings are not formed, but the plume is displaced out of the mine via the standing wave in the downstream direction. This transport mechanism is more noticeable for the shallow mine since the wave for the deep mine transports the plume higher in the surface layer, so that it would not be probed at 10 m above grade. Another interesting note is the asymmetric structure of the flow and passive scalar fields in the span-wise direction despite the symmetry of the topography in that direction. Such a feature was also noted by Flores et al. (2014), who showed the asymmetry of plume dispersion for a symmetric circular mine (their Figs. 6 and 7).

3.2.1. *Surface-layer profiles*

Fig. 10 shows the profiles of normalized mean x-component wind velocity outside (P1 to P10) and inside (P11 to P13) the shallow and deep mines. For this normalization the friction velocity at 10 m alitute on P3 is chosen. The velocity component increases downstream of the mine in the lower portion of the surface layer ($z < 50$ m), in agreement with the observation of Nahian et al. (2020) (their Fig. 5a), who measured enhanced up-slope winds over the edge of a mine comparable to the shallow mine. Examining the profiles inside the mine (P11 to P13), it can be seen that for the shallow mine, back flows (or circulations) occur under most thermal stability conditions, where $\overline{U}_x < 0$ on one or more of such profiles. Such circulations have been also predicted by Nahian et al. (2020) (their Fig. 7e). On the other hand, back flow is predicted to enhance for the deep mine case. Similar back flow conditions were predicted by simulations of Flores et al. (2014) in a deep mine under the thermally neutral and unstable conditions (their Fig. 3a and e).

Fig. 11 shows the profiles of normalized mean z-component of the wind velocity outside (P1 to P10) and inside (P11 to P13) the shallow and deep mines. The most notable mean advective flow in the vertical direction is associated with the deep mine under the thermally stable conditions. The vertical motion is best described by the standing wave formation. Here on the lee side of the mine (P11) warm air is transported from aloft toward the bottom of the mine ($\overline{U}_z < 0$), while the rising flow due to this standing wave is notable on the center of the mine (P12), wind side of the mine (P13), and downstream of the mine (P6) ($\overline{U}_z > 0$). A similar flow structure was observed by Lehner et al. (2016) (their Figs. 2b and 10) associated with a natural earth depression comparable to the deep mine. Clements et al. (2003) and Lehner et al. (2016) characterized the wave in such a way that areas of strong wind are remained relatively confined, with comparatively weak wind speeds above the descending flow and quiescent conditions in the center of the mine below the wave crest (Fig. 10 in Lehner et al. (2016)).

Fig. 12 shows the change in potential temperature profiles from the surface outside (P1 to P10) and inside (P11 to P13) the shallow and deep mines. In the upstream of the mine, the thermally unstable ($\partial\overline{\Theta}/\partial z < 0$), neutral ($\partial\overline{\Theta}/\partial z \sim 0$), and stable ($\partial\overline{\Theta}/\partial z > 0$) conditions can be distinguished near the surface ($z < 25$ m). However, inside and downstream of the mine the profiles of the mean potential temperature become more uniform, particularly under the thermally stable conditions. This is indicative of turbulent and advective mixing in these regions, which result in more uniform distribution of potential temperature in the vertical direction. The tendency of the formation of the isothermal layer is hypothesized to be due to air circulations and mixing inside the mine

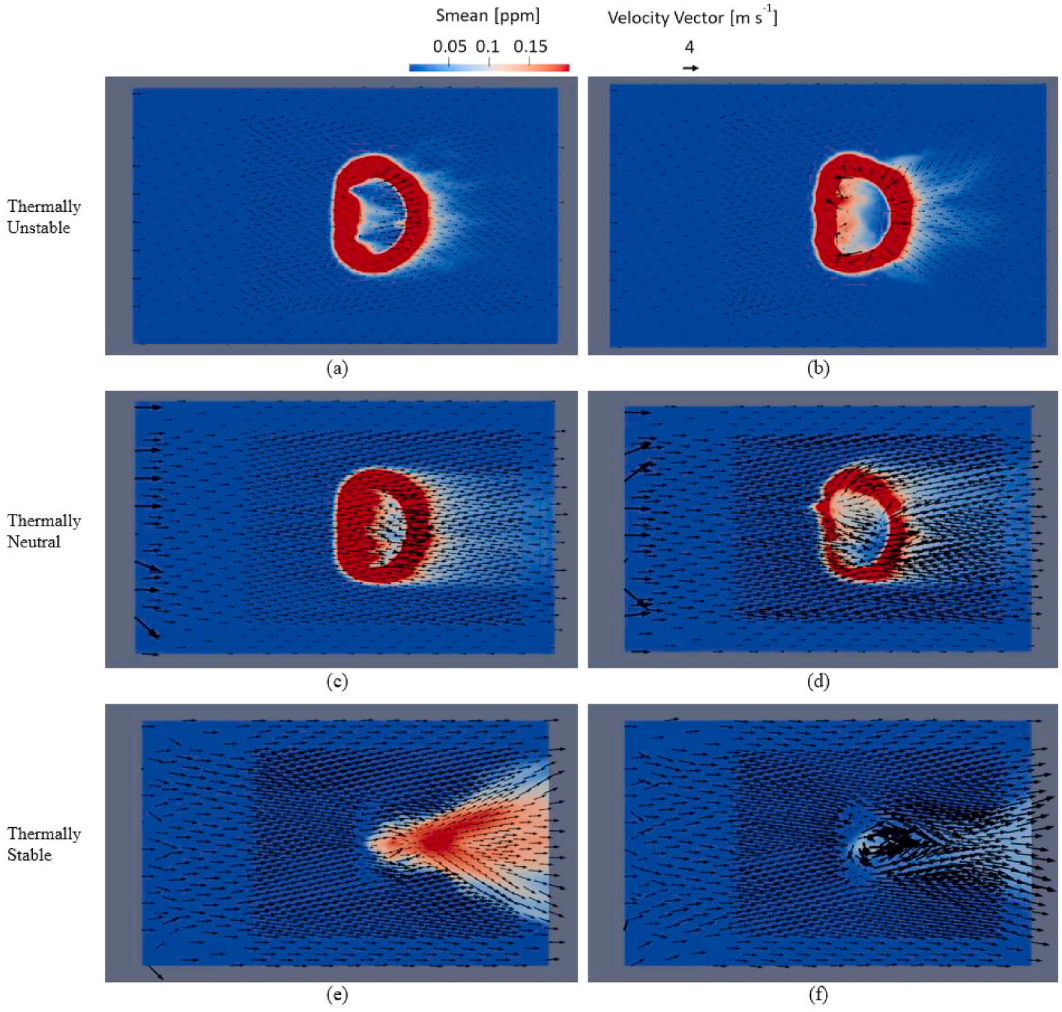

Fig. 9. Wind field velocity vectors and passive scalar contours for thermally unstable (a and b), thermally neutral (c and d), and thermally stable (e and f) cases for the shallow (a, c, e) and deep (b, d, f) mines on a horizontal cross section at 10 m above grade.

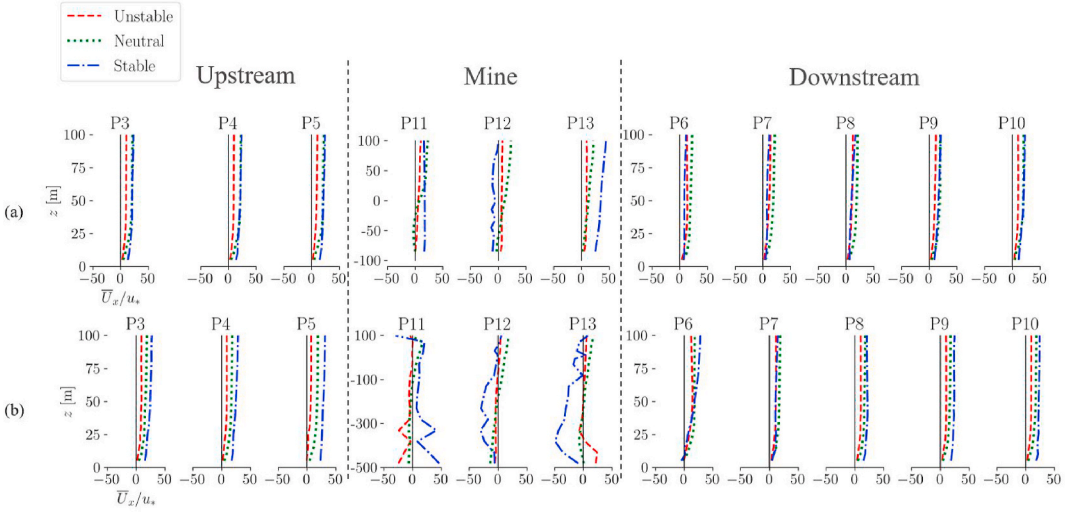

Fig. 10. Profiles of normalized mean velocity in the *x*-direction ($\overline{U}_x$) outside (P1 to P10) and inside (P11 to P13) the mine for different thermal stability cases and topographies; a) shallow and b) deep mines.

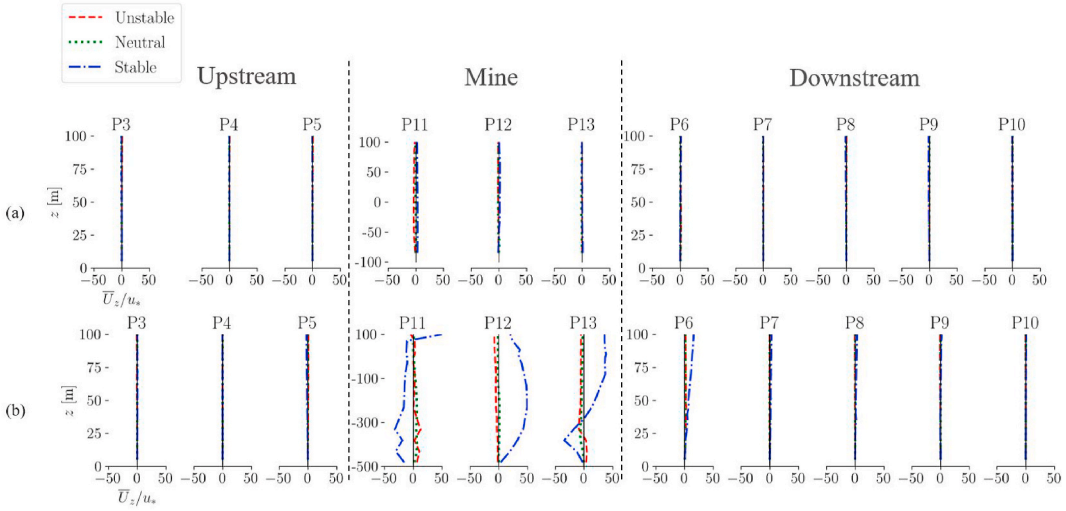

Fig. 11. Profiles of normalized mean velocity in the z-direction ($\overline{U}_z$) outside (P1 to P10) and inside (P11 to P13) the mine for different thermal stability cases and topographies; a) shallow and b) deep mines.

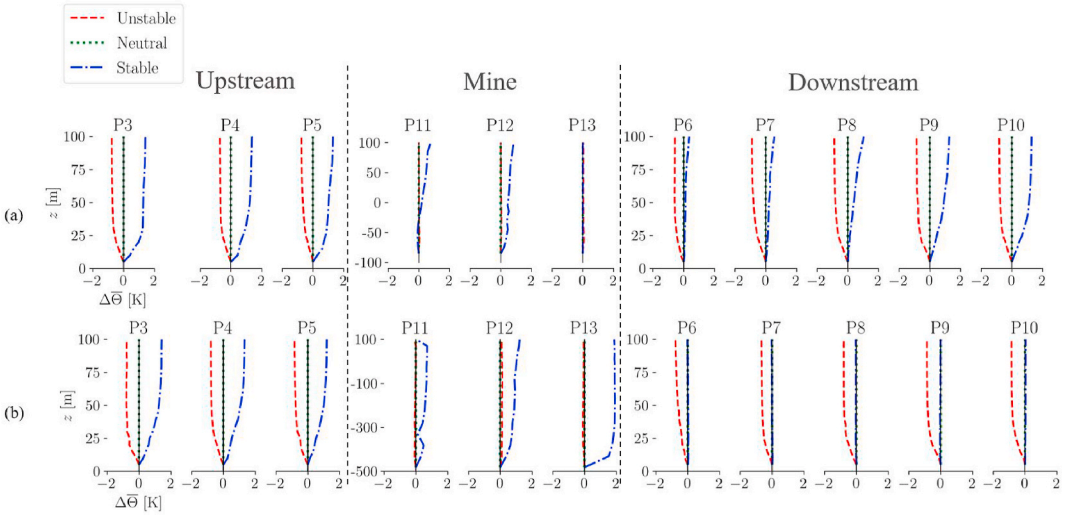

Fig. 12. Profiles of change in mean potential temperature from the surface ($\overline{\Theta}$) outside (P1 to P10) and inside (P11 to P13) the mine for different thermal stability cases and topographies; a) shallow and b) deep mines.

and air incursions across the depression edge (Whiteman et al., 2008). Particularly during the thermally stable conditions, similar potential temperature profiles were observed by Nahian et al. (2020) (their Fig. 5b) and Clements et al. (2003) (their Figs. 5, 8 and 9), Whiteman et al. (2008) (their Fig. 10), and Lehner et al. (2016) (their Fig. 8).

The normalized mean passive scalar mixing ratio profiles outside (P1 to P10) and inside (P11 to P13) the shallow and deep mines are presented in Fig. 13. In agreement with Fig. 8, under thermally unstable and neutral cases the flow structure in the mine causes a back flow so that the passive scalar is transported upstream, and it is detected on P5. The back flow is the direct consequence of flow circulation inside the mine closer to the lee side, where $\overline{U}_x < 0$ on P11 in Fig. 10. Under the thermally stable conditions, however, no propagation of the passive scalar is predicted upstream. On the downstream side of the mine several features can be noted. Under the thermally neutral case, simulations for both the shallow and deep mines show a thin passive scalar plume limited to the lower part of the surface layer ($z < 25$ m) on P6, which is diluted on the subsequent profiles. This is the artifact of the skimming flow. Under the thermally unstable case, the deep mine simulations show greater level of mixing so that the plume reaches higher in the surface layer on P6. For both the shallow and deep mines the plume is diluted on the subsequent profiles due to enhanced mixing downstream of the mines. The most interesting feature is the structure of the plume downstream of the mines under the thermally stable conditions. In agreement with Fig. 8, for the shallow mine, the plume is predicted to rise at a short distance downstream of the mine ($\overline{U}_z > 0$ on P6 in Fig. 11) to cover the majority of the surface layer on P6; however, on subsequent profiles, subsiding flow occurs ($\overline{U}_z < 0$ on P8 and P9 in Fig. 11) that cause the plume to be detected only on the lower portion of the surface layer ($z < 25$ m) on P8 and P9. For the deep mine, and due to the standing wave transporting the plume above the surface layer downstream of the mine, no indication of the plume is noted on P6 to P10, possibly due to advective transport and turbulent mixing that result in displacement and dilution of the plume upward, respectively.

The profiles of normalized turbulent sensible kinematic vertical heat flux outside (P1 to P10) and inside (P11 to P13) the shallow and deep mines are presented in Fig. 14. Upstream of the mine, the positive heat flux can be noted for the thermally unstable case and negative heat flux for the thermally stable case (P3 to P5), which are typical of surface layers over flat and homogeneous lands. Most notably, the mines

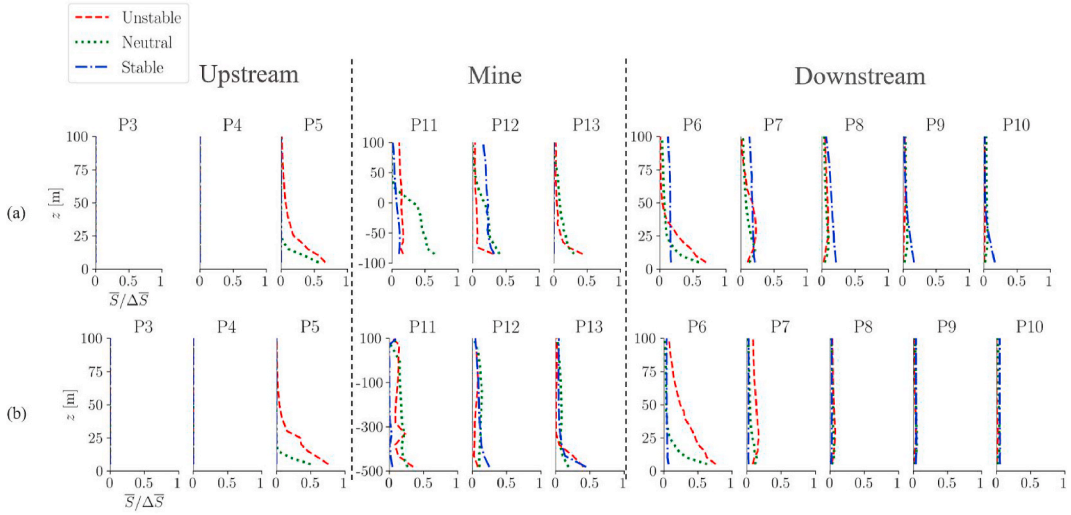

Fig. 13. Profiles of normalized mean mixing ratio ($\overline{S}$) outside (P1 to P10) and inside (P11 to P13) the mine for different thermal stability cases and topographies; a) shallow and b) deep mines.

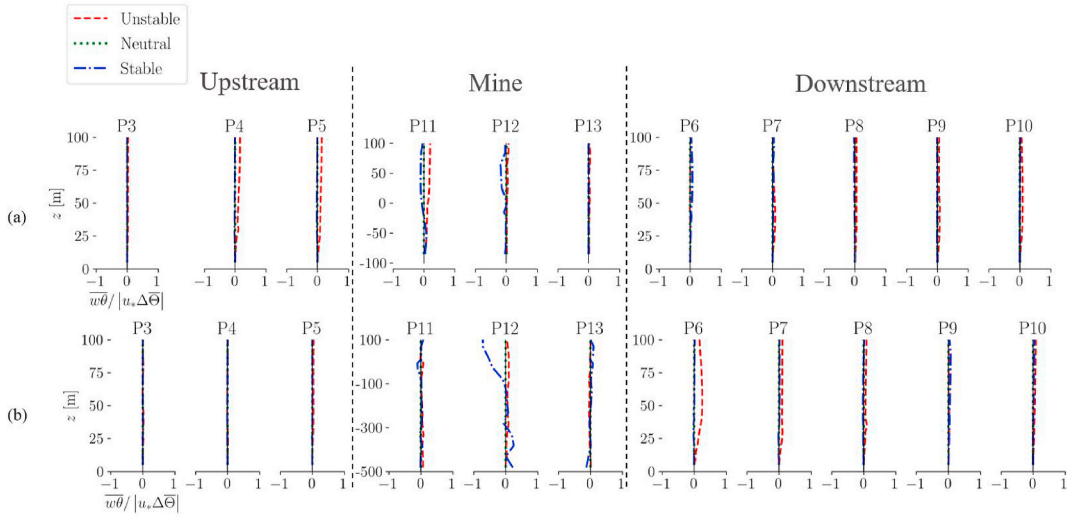

Fig. 14. Profiles of normalized turbulent sensible kinematic vertical heat flux ($\overline{w\theta}$) outside (P1 to P10) and inside (P11 to P13) the mine for different thermal stability cases and topographies; a) shallow and b) deep mines.

influence the magnitude and sign of the heat flux under the thermally stable case. For the shallow mine, it is observed that the magnitude of the negative heat flux is enhanced near the top of the surface layer on profiles P11 and P12. This could be due to formation of a shear layer and enhanced turbulence at this height. The heat flux on the downstream side becomes positive, possibly due to the subsiding of warm air into the mine and its rise downstream. For the deep mine, the presence of the standing wave and its influence on the heat flux can be noted on profile P12. Near the bottom of this profile, the heat flux is positive, due to the subsidence of warm air from aloft that reaches the wave bottom and contributes to an overall warming due to vertical turbulent exchange. Near the top of this profile, the heat flux is negative, due to interaction of the wave crest with cold stream of air above with an overall cooling due to vertical turbulent exchange.

Figs. 15–17 show the normalized resolved, SGS, and total TKE, i.e. k_{res}, k_{sgs}, and k_{tot}, respectively, outside (P1 to P10) and inside (P11 to P13) the shallow and deep mines. Note that the total kinetic energy is the sum of the resolved and SGS parts, i.e. $k_{tot} = k_{res} + k_{sgs}$. The percentage of k_{res} out of k_{tot} is a critical parameter to evaluate the capability of an LES method to simulate fluctuating eddies and their role in transport phenomena (Rasam et al., 2011). In economized VLES methods equipped with wall functions, it is acceptable to model a great fraction of k_{tot} near the walls, while typically greater than 60–80% of k_{tot} shall be resolved away from the walls (Aliabadi et al., 2018). This condition is met by the model, where above $z = 25$ m, most of k_{tot} is resolved. This pattern can be seen from Figs. 15 and 16. The fraction of k_{tot} resolved on profile P8 is calculated, as the flow field is fully developed at this location downstream of the mine where the effects of the mine and thermal stability conditions have been experienced by the flow. For this profile, on average for all three stability conditions for the shallow mine, between 65 and 75% of k_{tot} is resolved in elevations from $z = 25$ m to $z = 50$ m. Examining locations above $z = 50$ m, the simulation results show that even a greater portion of k_{tot} is resolved. The average fraction of k_{tot} resolved for the deep mine in all thermal stability conditions is about 90% above $z = 25$ m.

Focusing on the profiles in Fig. 17, it is noted that in both shallow and deep mine cases, higher levels of k_{tot} exist inside the pit compared to the outside. This can be an artifact for the presence of sloped flow, circulations, shear layer, and other complex flow phenomena that generate turbulence. Furthermore, the stepped walls of the mine contribute to

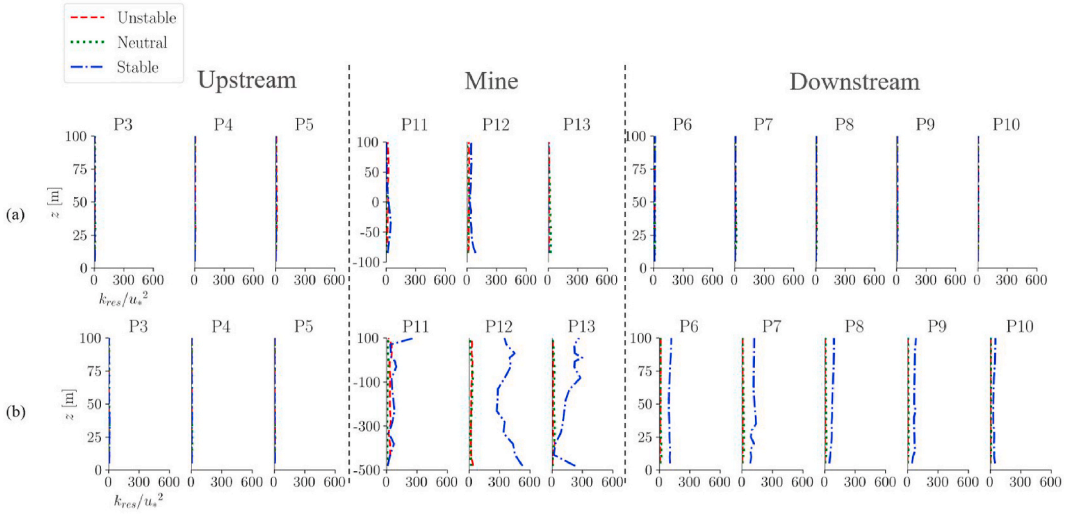

Fig. 15. Profiles of the normalized resolved TKE (k_{res}) outside (P1 to P10) and inside (P11 to P13) the mine for different thermal stability cases and topographies; a) shallow and b) deep mines.

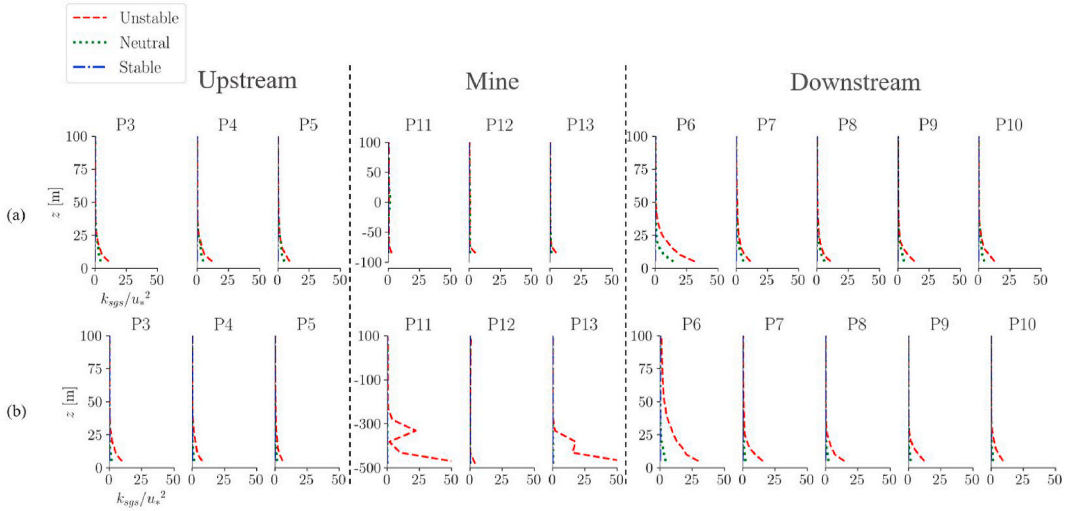

Fig. 16. Profiles of the normalized sub-grid TKE (k_{sgs}) outside (P1 to P10) and inside (P11 to P13) the mine for different thermal stability cases and topographies; a) shallow and b) deep mines.

increasing the surface roughness and turbulence. The enhancement of k_{tot} inside earth depressions have also been predicted by Silvester et al. (2009) and Aliabadi et al. (2017). A higher amount of k_{tot} is predicted in the deep mine compared to the shallow mine, possibly due to more abrupt topographical changes and enhancement of circulations. Downstream of the shallow mine, and under the thermally unstable conditions, a local peak for k_{tot} is predicted on profiles P7 to P9 at about $z =$ 25 m, which is indicative of a shear layer and a local low-level jet caused by topography.

Fig. 18 shows the profiles of normalized advective plus turbulent flux of the passive scalar in the x-direction ($\overline{US} + \overline{us}$) outside (P1 to P10) and inside (P11 to P13) the shallow and deep mines. Under the thermally unstable and neutral conditions, the back flow caused by the flow circulation in the mines results in a positive flux upstream of the mines on P5 below $z = 15$ m in both cases. Inside the deep mine, the formation of a circulation of plume under the thermally unstable conditions is evident. The circulation pushes the passive scalar toward the mine wall and causes the passive scalar to exit from the lee side (P11) and wind side (P13) of the deep mine. A similar pattern of particle movements inside a deep mine has been predicted by Flores et al. (2014) (their Fig. 7c and e).

The downstream profiles under the thermally unstable conditions show a thin plume under $z = 40$ m for both shallow and deep mines (P6). These results are in agreement with those of Flores et al. (2014), who also showed that in a deep mine, the plume height after the pit is higher under thermally unstable conditions than the thermally neutral conditions (their Fig. 7a and e). Again, due to the standing wave formed for the deep mine under the thermally stable condition, no notable flux can be predicted downstream of the mine in the surface layer. The flux is rather distributed over a significant portion of the boundary layer.

Fig. 19 shows the profiles of normalized advective plus turbulent flux of the passive scalar in the z-direction ($\overline{WS} + \overline{ws}$) outside (P1 to P10) and inside (P11 to P13) the shallow and deep mines. The most notable feature here is the impact of the standing wave on the flux for the deep mine under the thermally stable condition. Here a large component of the vertical flux is predicted at the center of the mine on profile P12. This is due to the rising structure of air that transports the passive scalar vertically out of the mine.

The flow complexities noted here warrant a closer investigation of diagnostic meteorological models based on the Gaussian plume dispersion paradigm. It is expected that the Gaussian plume models yield

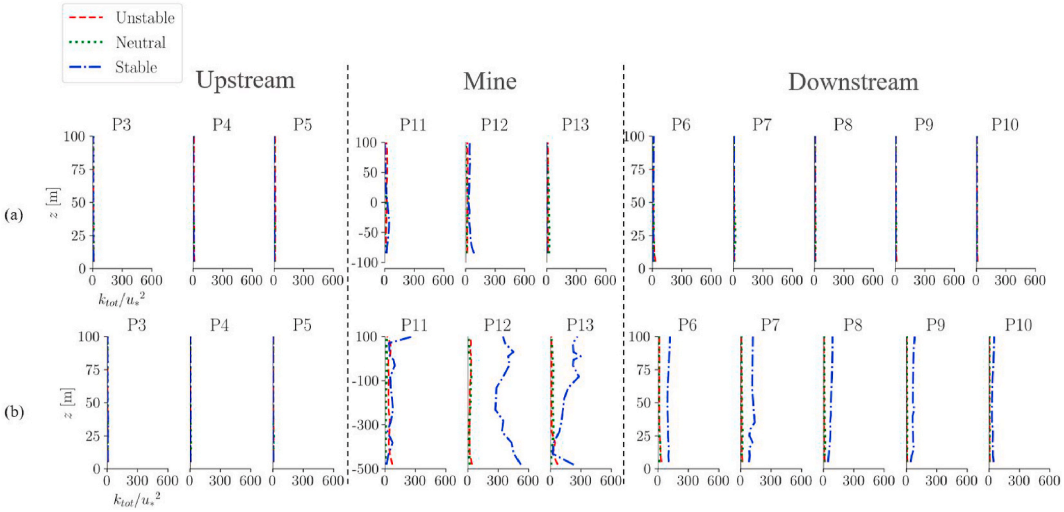

Fig. 17. Profiles of the normalized total TKE ($k_{tot} = k_{res} + k_{sgs}$) outside (P1 to P10) and inside (P11 to P13) the mine for different thermal stability cases and topographies; a) shallow and b) deep mines.

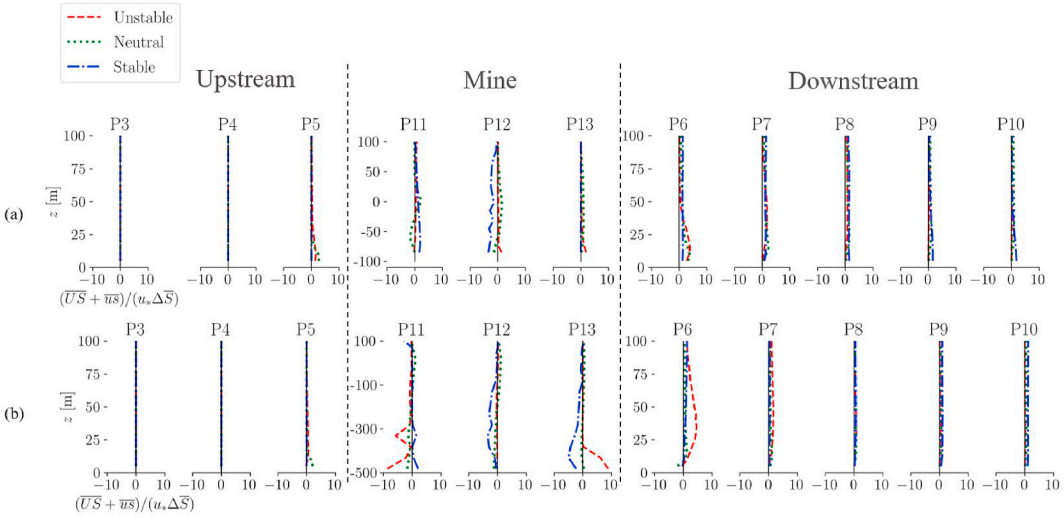

Fig. 18. Profiles of normalized advective plus turbulent flux of passive scalar in the *x*-direction ($\overline{US} + \overline{us}$) outside (P1 to P10) and inside (P11 to P13) the mine for different thermal stability cases and topographies; a) shallow and b) deep mines.

dispersion results substantially different from those predicted using this CFD analysis, particularly if they attempt to predict dispersion transport over complex terrain with topographical unevenness.

4. Conclusions and recommendations

In this study atmospheric flow and transport were simulated using Computational Fluid Dynamics (CFD) inside and surrounding two synthetic open-pit mines of different depths under different thermal stability conditions. A Very Large Eddy Simulation (VLES) method was used, which was capable of resolving the turbulent fluctuations in the interior of the domain, while modeling transport phenomena near walls using wall functions. The main objective was to investigate the effects of mine depth and thermal stability on the flow structure and dispersion of a fugitive passive scalar released from the surface of the mines. Six simulations were conducted for two mine depths: a shallow (~ 100 m) and a deep (~ 500 m) mine; and three thermal stability conditions aimed at matching the friction velocity u_* and Obukhov length L from an observation dataset: thermally unstable ($u_* = 0.25$ m s^{-1}, $L = -11$ m), thermally neutral ($u_* = 0.46$ m s^{-1}), and thermally stable ($u_* = 0.12$ m s^{-1}, $L = 9$ m) conditions. The CFD model was evaluated against field observations within the surface layer upstream of the mines to gain confidence on its predictions.

For the shallow mine, the following predictions were made. Under thermally unstable conditions substantial mixing and rising of the passive scalar plume occurred downstream of the mine, so that the plume was diluted and had a depth that reached a large portion of the Atmospheric Boundary Layer (ABL). Under thermally neutral conditions, skimming flow was predicted, and the plume rise was limited to the surface layer downstream of the mine. Substantial circulation of flow inside the mine was predicted under both thermally unstable and neutral conditions. Under the thermally stable conditions, less flow circulation was predicted inside the mine, and the plume rise was limited to the surface layer downstream of the mine.

For the deep mine under thermally unstable conditions substantial mixing and rising of the passive scalar plume occurred downstream of the mine, so that the plume was diluted and covered within a greater portion of the ABL than the other thermal stability cases. Also, under thermally neutral conditions, the skimming flow was predicted, restricting the plume to the surface layer down stream of the mine. In the

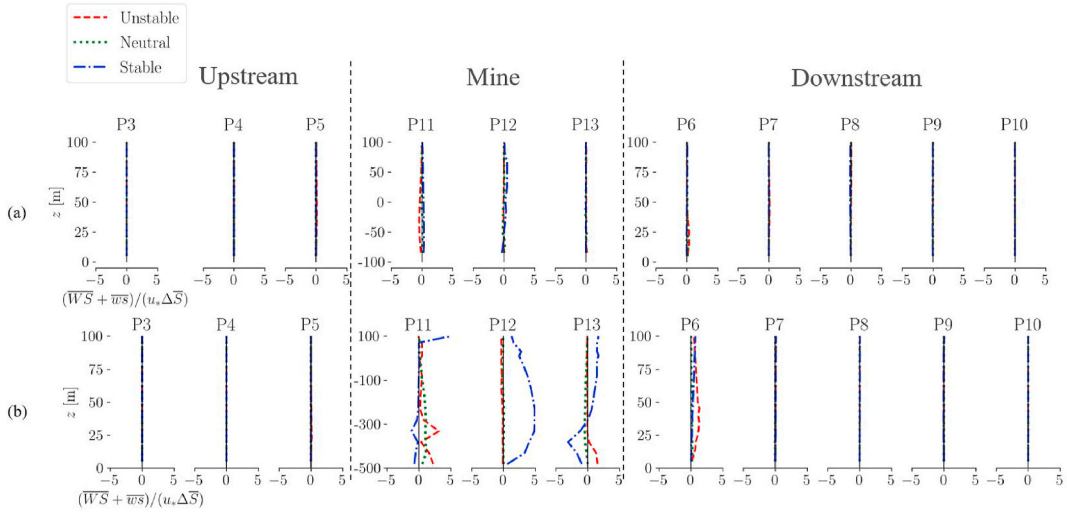

Fig. 19. Profiles of normalized advective plus turbulent flux in the z-direction ($\overline{WS}+\overline{ws}$) outside (P1 to P10) and inside (P11 to P13) the mine for different thermal stability cases and topographies; a) shallow and b) deep mines.

stable case a standing wave formed, which brought warm air from aloft upstream of the mine into the bottom of the mine, and a rising flow structure transported the passive scalar upward from the center of the mine into the ABL above surface layer.

Predictions of transport phenomena by the VLES method associated with the depth of the mines and thermal stability conditions were reported in this study. The meteorological flow fields predicted by this VLES method can be ingested in other operational tools for more accurate estimates of air pollution dispersion and emission flux from complex terrains. In addition, the model can be used stand-alone for future assessment of transport phenomena inside and surrounding real mines. Given the flow complexities noted in this study, a follow-up study is planned, where the CFD results will be compared, as a benchmark, to the results of diagnostic meteorological models based on the Gaussian plume dispersion paradigm, which are commonly used in the industry.

Despite the advantages, the VLES method has some limitations for real investigations that require further research. This model cannot simulate very low wind speed conditions, which is a characteristic of some thermally stable boundary layers at nighttime. This application would require further research and development for the model. The inlet boundary conditions for the model need to be carefully adapted for each atmospheric state. The model cannot incorporate horizontal variations of meteorological fields at meso scale (wind direction change, meandering, etc.) so there are limitations on the scale at which the model can be used successfully. To be used at larger scales, the model may be coupled or nested with the Weather Research and Forecasting (WRF) model for appropriate specification of inlet and boundary conditions.

5. Availability of code and data

The Atmospheric Innovations Research (AIR) Laboratory at the University of Guelph may provide the confidential supporting field data via the authorization of the data owners. The AIR lab will provide the model source code upon request. For access, contact Principal Investigator Amir A. Aliabadi (aliabadi@uoguelph.ca).

CRediT authorship contribution statement

Seyedahmad Kia: Data curation, Formal analysis, Investigation, Methodology, Validation, Visualization, Writing – original draft. **Thomas K. Flesch:** Conceptualization, Data curation, Investigation, Methodology, Supervision, Writing – review & editing. **Brian S. Freeman:** Supervision, Writing – review & editing. **Amir A. Aliabadi:** Conceptualization, Data curation, Formal analysis, Funding acquisition, Investigation, Methodology, Supervision, Writing – review & editing.

Declaration of competing interest

The authors declare that they have no known competing financial interests or personal relationships that could have appeared to influence the work reported in this paper.

Acknowledgments

The Tethered Air Blimp (TAB) was partially developed by the assistance of Denis Clement, Jason Dorssers, Katharine McNair, James Stock, Darian Vyriotes, Amanda Pinto, and Phillip Labarge. The authors thank Andrew F. Byerlay for designing and constructing the tether reel system for TAB. The authors thank Nikolaos Veriotes and Manoj K. Nambiar for field assistance in collecting environmental data. The authors are indebted to Steve Nyman, Chris Duiker, Peter Purvis, Manuela Racki, Jeffrey Defoe, Joanne Ryks, Ryan Smith, James Bracken, and Samantha French at the University of Guelph, who helped with the campaign logistics. Special credit is directed toward Amanda Sawlor, Datev Dodkelian, Esra Mohamed, Di Cheng, Randy Regan, Margaret Love, and Angela Vuk at the University of Guelph for administrative support. The computational platforms were set up with the assistance of IT staff Jeff Madge, Joel Best, and Matthew Kent at the University of Guelph. In-kind technical support for this work was provided by Rowan Williams Davies and Irwin, Inc. (RWDI). Technical guidance from John D. Wilson from University of Alberta is appreciated.

This work was supported by the University of Guelph, Ed McBean philanthropic fund; the Discovery Grant program (401231) from the Natural Sciences and Engineering Research Council (NSERC) of Canada; Government of Ontario through the Ontario Centres of Excellence (OCE) under the Alberta-Ontario Innovation Program (AOIP) (053450); and Emission Reduction Alberta (ERA) (053498). OCE is a member of the Ontario Network of Entrepreneurs (ONE). The lead author was partially financially supported by the University of Guelph.

References

Ahmadi-Baloutaki, M., Aliabadi, A.A., 2021. A very large-eddy simulation model using a reductionist inlet turbulence generator and wall modelling for stable atmospheric boundary layers. Fluid Dynam. 56, 413–432. https://doi.org/10.1134/S0015462821020026.

Aliabadi, A.A., 2018. Theory and Applications of Turbulence: A Fundamental Approach for Scientists and Engineers. Amir A. Aliabadi Publications, Guelph, Ontario, Canada.
Aliabadi, A.A., Krayenhoff, E.S., Nazarian, N., Chew, L.W., Armstrong, P.R., Afshari, A., Norford, L.K., 2017. Effects of roof-edge roughness on air temperature and pollutant concentration in urban canyons. Bound.-Lay. Meteorol. 164, 249–279. https://doi.org/10.1007/s10546-017-0246-1.
Aliabadi, A.A., Veriotes, N., Pedro, G., 2018. A Very Large-Eddy Simulation (VLES) model for the investigation of the neutral atmospheric boundary layer. J. Wind Eng. Ind. Aerod. 183, 152–171. https://doi.org/10.1016/j.jweia.2018.10.014.
Aliabadi, A.A., Moradi, M., Clement, D., Lubitz, W.D., Gharabaghi, B., 2019. Flow and temperature dynamics in an urban canyon under a comprehensive set of wind directions, wind speeds, and thermal stability conditions. Environ. Fluid Mech. 19, 81–109. https://doi.org/10.1007/s10652-018-9606-8.
Baklanov, A.A., 1995. Numerical modelling of atmosphere processes in mountain cirques and open pits. WIT Trans. Ecol. Environ. 9, 8. https://doi.org/10.2495/AIR950271.
Baklanov, A.A., 2000. Application of CFD methods for modelling in air pollution problems: possibilities and gaps. Environ. Monit. Assess. 65, 181–189. https://doi.org/10.1007/978-94-010-0932-4_20.
Baray, S., Darlington, A., Gordon, M., Hayden, K.L., Leithead, A., Li, S.M., Liu, P.S.K., Mittermeier, R.L., Moussa, S.G., O'Brien, J., Staebler, R., Wolde, M., Worthy, D., McLaren, R., 2018. Quantification of methane sources in the Athabasca oil sands region of Alberta by aircraft mass balance. Atmos. Chem. Phys. 18, 7361–7378. https://doi.org/10.5194/acp-18-7361-2018.
Benhamadouche, S., Jarrin, N., Addad, Y., Laurence, D., 2006. Synthetic turbulent inflow conditions based on a vortex method for large-eddy simulation. Prog. Comput. Fluid Dynam. Int. J. 6, 50–57. https://doi.org/10.1504/PCFD.2006.009482.
Bhowmick, T., 2015. Three Dimensional Computational Fluid Dynamics Models of Fugitive Dust Dispersion in High-Latitude Open-Pit Mines. Master's thesis. University of Alaska Fairbanks, USA.
Bhowmick, T., Bandopadhyay, S., Ghosh, T., 2015. Three-dimensional CFD modeling approach to approximate air pollution conditions in high-latitude open-pit mines. WIT Trans. Built Environ. 168, 741–753. https://doi.org/10.2495/SD150652.
Blocken, B., Stathopoulos, T., Carmeliet, J., 2007. CFD simulation of the atmospheric boundary layer: wall function problems. Atmos. Environ. 41, 238–252. https://doi.org/10.1016/j.atmosenv.2006.08.019.
Brés, G.A., Colonius, T., 2008. Three dimensional instabilities in compressible flow over open cavities. J. Fluid Mech. 599, 309–339. https://doi.org/10.1017/S0022112007009925.
Byerlay, R.A.E., Nambiar, M.K., Nazem, A., Nahian, M.R., Biglarbegian, M., Aliabadi, A.A., 2020. Measurement of land surface temperature from oblique angle airborne thermal camera observations. Int. J. Rem. Sens. 41, 3119–3146. https://doi.org/10.1080/01431161.2019.1699672.
Cheng, W., Liu, C.-H., 2011. Large-eddy simulation of turbulent transports in urban street canyons in different thermal stabilities. J. Wind Eng. Ind. Aerod. 99, 434–442. https://doi.org/10.1016/j.jweia.2010.12.009.
Choudhury, A., Bandopadhyay, S., 2016. The effect of overall pit slope and pit geometry on the dispersion of pollutants in a hypothetical arctic open-pit mine. Nat. Resour. Eng. 1, 26–34. https://doi.org/10.1080/23802693.2016.1231499.
Clements, C.B., Whiteman, C.D., Horel, J.D., 2003. Cold-air-pool structure and evolution in a mountain basin: Peter Sinks, Utah. J. Appl. Meteorol. 42, 752–768. https://doi.org/10.1175/1520-0450(2003)042\%3C0752:CSAEIA\%3E2.0.CO;2.
Flesch, T.K., Prueger, J.H., Hatfield, J.L., 2002. Turbulent Schmidt number from a tracer experiment. Agric. For. Meteorol. 111, 299–307. https://doi.org/10.1016/S0168-1923(02)00025-4.
Flores, F., Garreaud, R., Muñoz, R.C., 2013. CFD simulations of turbulent buoyant atmospheric flows over complex geometry: solver development in OpenFOAM. Comput. Fluids 82, 1–13. https://doi.org/10.1016/j.compfluid.2013.04.029.
Flores, F., Garreaud, R., Muñoz, R.C., 2014. OpenFOAM applied to the CFD simulation of turbulent buoyant atmospheric flows and pollutant dispersion inside large open pit mines under intense insolation. Comput. Fluids 90, 72–87. https://doi.org/10.1016/j.compfluid.2013.11.012.
Gavrilov, K.A., Morvan, D., Accary, G., Lyubimov, D.V., Meradji, S., Bessonov, O.A., 2011. Numerical modeling of coherent structures attendant on impurity propagation in the atmospheric boundary layer over a forest canopy. Fluid Dynam. 46, 138–147. https://doi.org/10.1134/S0015462811010169.
Ghoreishi-Madiseh, S.A., Sasmito, A.P., Hassani, F.P., Amiri, L., 2017. Performance evaluation of large scale rock pit seasonal thermal energy storage for application in underground mine ventilation. Appl. Energy 185, 1940–1947. https://doi.org/10.1016/j.apenergy.2016.01.062.
Gordon, M., Li, S.-M., Staebler, R., Darlington, A., Hayden, K., O'Brien, J., Wolde, M., 2015. Determining air pollutant emission rates based on mass balance using airborne measurement data over the Alberta oil sands operations. Atmos. Meas. Technol. 8, 3745–3765. https://doi.org/10.5194/amt-8-3745-2015.
Greenshields, C.J., 2016. OpenFOAM: the Open Source CFD Toolbox, User Guide. Technical Report OpenFOAM Foundation Ltd, London, W13 3DB, United Kingdom. PO Box 56676, Version 4.0.
Gualtieri, C., Angeloudis, A., Bombardelli, F., Jha, S., Stoesser, T., 2017. On the values for the turbulent Schmidt number in environmental flows. Fluids 2, 17. https://doi.org/10.3390/fluids2020017.
Han, Y., Stoellinger, M., Naughton, J., 2016. Large-eddy simulation for atmospheric boundary layer flow over flat and complex terrains. J. Phys. Conf. Ser. 753, 032044 https://doi.org/10.1088/1742-6596/753/3/032044.
Han, B.S., Baik, J.-J., Park, S.-B., Kwak, K.-H., 2019. Large-eddy simulations of reactive pollutant dispersion in the convective boundary layer over flat and urban-like surfaces. Bound.-Lay. Meteorol. 172, 271–289. https://doi.org/10.1007/s10546-019-00447-2.
Hansen, K.S., Barthelmie, R.J., Jensen, L.E., Sommer, A., 2012. The impact of turbulence intensity and atmospheric stability on power deficits due to wind turbine wakes at Horns Rev wind farm. Wind Energy 15, 183–196. https://doi.org/10.1002/we.512.
Huang, J., Bou-Zeid, E., 2013. Turbulence and vertical fluxes in the stable atmospheric boundary layer. Part I: a large-eddy simulation study. J. Atmos. Sci. 70, 1513–1527. https://doi.org/10.1175/JAS-D-12-0167.1.
Jayatillaka, C.L.V., 1969. The influence of Prandtl number and surface roughness on the resistance of the laminar sublayer to momentum and heat transfer. Prog. Heat Mass Transfer 1, 193–329.
Joseph, G.M.D., Lowndes, I.S., Hargreaves, D., 2018. A computational study of particulate emissions from Old Moor Quarry, UK. J. Wind Eng. Ind. Aerod. 172, 68–84. https://doi.org/10.1016/j.jweia.2017.10.018.
Kaimal, J.C., Wyngaard, J.C., Haugen, D.A., Coté, O.R., Izumi, Y., Caughey, S.J., Readings, C.J., 1976. Turbulence structure in the convective boundary layer. J. Atmos. Sci. 33, 2152–2169. https://doi.org/10.1175/1520-0469(1976)033<2152:TSITCB>2.0.CO;2.
Kang, W., Sung, H.J., 2009. Large-scale structures of turbulent flows over an open cavity. J. Fluid Struct. 25, 1318–1333. https://doi.org/10.1016/j.jfluidstructs.2009.06.005.
Kato, M., Hanafusa, T., 1996. Wind tunnel simulation of atmospheric turbulent flow over a flat terrain. Atmos. Environ. 30, 2853–2858. https://doi.org/10.1016/1352-2310(95)00310-X.
Katta, A.K., Davis, M., Kumar, A., 2020. Development of disaggregated energy use and greenhouse gas emission footprints in Canada's iron, gold, and potash mining sectors. Resour. Conserv. Recycl. 152, 104485. https://doi.org/10.1016/j.resconrec.2019.104485.
Kays, W.M., 1994. Turbulent Prandtl number. Where are we? J. Heat Trans.-T. ASME 116, 284–295.
Kays, W.M., Crawford, M.E., 1993. Convective Heat and Mass Transfer, third ed. McGraw-Hill Inc, New York.
Kim, H.G., Patel, V., Lee, C.M., 2000. Numerical simulation of wind flow over hilly terrain. J. Wind Eng. Ind. Aerod. 87, 45–60. https://doi.org/10.1016/S0167-6105(00)00014-3.
Koeltzsch, K., 2000. The height dependence of the turbulent Schmidt number within the boundary layer. Atmos. Environ. 34, 1147–1151. https://doi.org/10.1016/S1352-2310(99)00369-6.
Kumar, V., Kleissl, J., Meneveau, C., Parlange, M.B., 2006. Large-eddy simulation of a diurnal cycle of the atmospheric boundary layer: atmospheric stability and scaling issues. Water Resour. Res. 42, W06D09. https://doi.org/10.1029/2005WR004651.
Labois, M., Lakehal, D., 2011. Very-Large Eddy Simulation (V-LES) of the flow across a tube bundle. Nucl. Eng. Des. 241, 2075–2085. https://doi.org/10.1016/j.nucengdes.2011.02.009.
Lehner, M., Whiteman, C.D., Hoch, S.W., Crosman, E.T., Jeglum, M.E., Cherukuru, N.W., Calhoun, R., Adler, B., Kalthoff, N., Rotunno, R., Horst, T.W., Semmer, S., Brown, W.O.J., Oncley, S.P., Vogt, R., Grudzielanek, A.M., Cermak, J., Fonteyne, N.J., Bernhofer, C., Pitacco, A., Klein, P., 2016. The METCRAX II field experiment: a study of downslope windstorm-type flows in Arizona's Meteor Crater. Bull. Am. Meteorol. Soc. 97, 217–235. https://doi.org/10.1175/BAMS-D-14-00238.1.
Li, D., 2019. Turbulent Prandtl number in the atmospheric boundary layer-where are we now? Atmos. Res. 216, 86–105. https://doi.org/10.1016/j.atmosres.2018.09.015.
Li, X.-X., Britter, R.E., Koh, T.Y., Norford, L.K., Liu, C.-H., Entekhabi, D., Leung, D.Y.C., 2010. Large-eddy simulation of flow and pollutant transport in urban street canyons with ground heating. Bound.-Lay. Meteorol. 137, 187–204. https://doi.org/10.1007/s10546-010-9534-8.
Li, D., Katul, G.G., Zilitinkevich, S.S., 2015. Revisiting the turbulent Prandtl number in an idealized atmospheric surface layer. J. Atmos. Sci. 72, 2394–2410. https://doi.org/10.1175/JAS-D-14-0335.1.
Li, S.W., Hu, Z.Z., Chan, P.W., Hu, G., 2017. A study on the profile of the turbulence length scale in the near-neutral atmospheric boundary for sea (homogeneous) and hilly land (inhomogeneous) fetches. J. Wind Eng. Ind. Aerod. 168, 200–210. https://doi.org/10.1016/j.jweia.2017.06.008.
Liggio, J., Li, S.-M., Staebler, R.M., Hayden, K., Darlington, A., Mittermeier, R.L., O'Brien, J., McLaren, R., Wolde, M., Worthy, D., Vogel, F., 2019. Measured Canadian oil sands CO_2 emissions are higher than estimates made using internationally recommended methods. Nat. Commun. 10, 1863. https://doi.org/10.1038/s41467-019-09714-9.
Lin, C., Ooka, R., Kikumoto, H., Sato, T., Arai, M., 2021. CFD simulations on high-buoyancy gas dispersion in the wake of an isolated cubic building using steady RANS model and LES. Build. Environ. 188, 107478. https://doi.org/10.1016/j.buildenv.2020.107478.
Mahrt, L., Vickers, D., 2005. Boundary-layer adjustment over small-scale changes of surface heat flux. Bound.-Lay. Meteorol. 116, 313–330. https://doi.org/10.1007/s10546-004-1669-z.
Mahrt, L., Vickers, D., 2006. Extremely weak mixing in stable conditions. Bound.-Lay. Meteorol. 119, 19–39. https://doi.org/10.1007/s10546-005-9017-5.
Mathey, F., Cokljat, D., Bertoglio, J.P., Sergent, E., 2006. Assessment of the vortex method for large-eddy simulation inlet conditions. Prog. Comput. Fluid Dynam. Int. J. 6, 58–67. https://doi.org/10.1504/PCFD.2006.009483.
Maurer, V., Kalthoff, N., Wieser, A., Kohler, M., Mauder, M., Gantner, L., 2016. Observed spatiotemporal variability of boundary-layer turbulence over flat, heterogeneous terrain. Atmos. Chem. Phys. 16, 1377–1400. https://doi.org/10.5194/acp-16-1377-2016.
Medeiros, L.E., Fitzjarrald, D.R., 2014. Stable boundary layer in complex terrain. Part I: linking fluxes and intermittency to an average stability index. J. Appl. Meteorol. Clim. 53, 2196–2215. https://doi.org/10.1175/JAMC-D-13-0345.1.

Mellor, G.L., Yamada, T., 1974. A hierarchy of turbulence closure models for planetary boundary layers. J. Atmos. Sci. 31, 1791–1806. https://doi.org/10.1175/1520-0469(1974)031<1791:AHOTCM>2.0.CO;2.
Monin, A.S., Obukhov, A.M., 1954. Basic laws of turbulent mixing in the surface layer of the atmosphere. Contrib. Geophys. Inst. Acad. Sci. USSR 151, 163–187.
Moradi, M., Dyer, B., Nazem, A., Nambiar, M.K., Nahian, M.R., Bueno, B., Mackey, C., Vasanthakumar, S., Nazarian, N., Krayenhoff, E.S., Norford, L.K., Aliabadi, A.A., 2021. The vertical city weather generator (VCWG v1.3.2). Geosci. Model Dev. (GMD) 14, 961–984. https://doi.org/10.5194/gmd-14-961-2021.
Müller, P., 2006. The Equations of Oceanic Motions. Cambridge University Press, Cambridge, U.K.
Nahian, M.R., Nazem, A., Nambiar, M.K., Byerlay, R., Mahmud, S., Seguin, A.M., Robe, F. R., Ravenhill, J., Aliabadi, A.A., 2020. Complex meteorology over a complex mining facility: assessment of topography, land use, and grid spacing modifications in WRF. J. Appl. Meteorol. Clim. 59, 769–789. https://doi.org/10.1175/JAMC-D-19-0213.1.
Nambiar, M.K., Byerlay, R.A.E., Nazem, A., Nahian, M.R., Moradi, M., Aliabadi, A.A., 2020a. A Tethered Air Blimp (TAB) for observing the microclimate over a complex terrain. Geosci. Instrum. Meth. 9, 193–211. https://doi.org/10.5194/gi-9-193-2020.
Nambiar, M.K., Robe, F.R., Seguin, A.M., Endsin, M., Aliabadi, A.A., 2020b. Diurnal and seasonal variation of area-fugitive methane advective flux from an open-pit mining facility in Northern Canada using WRF. Atmosphere 11, 1227. https://doi.org/10.3390/atmos11111227.
Nieuwstadt, F.T.M., 1984. The turbulent structure of the stable, nocturnal boundary layer. J. Atmos. Sci. 41, 2202–2216. https://doi.org/10.1175/1520-0469(1984)041<2202:TTSOTS>2.0.CO;2.
Nozawa, K., Tamura, T., 2002. Large-eddy simulation of the flow around a low-rise building immersed in a rough-wall turbulent boundary layer. J. Wind Eng. Ind. Aerod. 90, 1151–1162. https://doi.org/10.1016/S0167-6105(02)00228-3.
Panofsky, H.A., Tennekes, H., Lenschow, D.H., Wyngaard, J.C., 1977. The characteristics of turbulent velocity components in the surface layer under convective conditions. Bound.-Lay. Meteorol. 11, 355–361. https://doi.org/10.1007/BF02186086.
Perrier, E.R., Robertson, J., Millington, R., Peters, D., 1972. Spatial and temporal variation of wind above and within a soybean canopy. Agric. Meteorol. 10, 421–442. https://doi.org/10.1016/0002-1571(72)90044-1.
Ponomarev, V.M., Chkhetiani, O.G., Shestakova, L.V., 2007. Nonlinear dynamics of large-scale vortex structures in a turbulent Ekman layer. Fluid Dynam. 42, 571–580. https://doi.org/10.1134/S0015462807040072.
Pope, S.B., 2000. Turbulent Flows. Cambridge University Press, Cambridge, U.K.
Qiu, X., Cheng, I., Yang, F., Horb, E., Zhang, L., Harner, T., 2018. Emissions databases for polycyclic aromatic compounds in the Canadian Athabasca oil sands region-development using current knowledge and evaluation with passive sampling and air dispersion modelling data. Atmos. Chem. Phys. 18, 3457–3467. https://doi.org/10.5194/acp-18-3457-2018.
Rajaratnam, N., 1990. Skimming flow in stepped spillways. J. Hydraul. Eng. 116, 587–591. https://doi.org/10.1061/(ASCE)0733-9429(1990)116:4(587).
Rasam, A., Brethouwer, G., Schlatter, P., Li, Q., Johansson, A.V., 2011. Effects of modelling, resolution and anisotropy of subgrid-scales on large-eddy simulations of channel flow. J. Turbul. N10. https://doi.org/10.1080/14685248.2010.541920.
Raupach, M.R., Antonia, R.A., Rajagopalan, S., 1991. Rough-wall turbulent boundary layers. Appl. Mech. Rev. 44, 1–25. https://doi.org/10.1115/1.3119492.
Reynolds, A.J., 1975. The prediction of turbulent Prandtl and Schmidt numbers. Int. J. Heat Mass Tran. 18, 1055–1069. https://doi.org/10.1016/0017-9310(75)90223-9.
Rodovalho, E., Quaglio, O., Flesch Junior, W.S., Pascual, R., de Tomi, G., Soares Tenório, J.A., 2020. Reducing GHG emissions through efficient tire consumption in open pit mines. J. Clean. Prod. 255, 120185. https://doi.org/10.1016/j.jclepro.2020.120185.
Roth, M., 2000. Review of atmospheric turbulence over cities. Q. J. Roy. Meteorol. Soc. 126, 941–990. https://doi.org/10.1002/qj.49712656409.
Sandham, J., Waite, M.L., 2015. Spectral energy balance in dry convective boundary layers. J. Turbul. 16, 650–675. https://doi.org/10.1080/14685248.2015.1023986.
Sergent, M.E., 2002. Vers une méthodologie de couplage entre la simulation des grandes echelles et les modéles statistique.
Shi, Y., Feng, X.S., Wei, F.S., Jiang, W., 2000. Three dimensional nonhydrostatic numerical simulation for the PBL of an open pit mine. Bound-Lay. Meteorol. 94, 197–224. https://doi.org/10.1023/A:1002404106737.
Silvester, S.A., Lowndes, I.S., Hargreaves, D.M., 2009. A computational study of particulate emissions from an open pit quarry under neutral atmospheric conditions. Atmos. Environ. 43, 6415–6424. https://doi.org/10.1016/j.atmosenv.2009.07.006.
Speziale, C., 1998. Turbulence modeling for time-dependent RANS and VLES: a review. Am. Inst. Aeronaut. Astronaut. J. 36, 173–184. https://doi.org/10.2514/2.7499.
Stull, R.B., 1988. An Introduction to Boundary Layer Meteorology. Kluwer Academic Publishers, Dordrecht, The Netherlands. https://doi.org/10.1007/978-94-009-3027-8.
Thé, J., Yu, H., 2017. A critical review on the simulations of wind turbine aerodynamics focusing on hybrid RANS-LES methods. Energy 138, 257–289. https://doi.org/10.1016/j.energy.2017.07.028.
Thomas, T.G., Williams, J.J.R., 1999. Generating a wind environment for large-eddy simulation of bluff body flows. J. Wind Eng. Ind. Aerod. 82, 189–208. https://doi.org/10.1016/S0167-6105(99)00037-9.
Tukkaraja, P., Keerthipati, M., French, A., 2016. Simulating temperature inversions in surface mines using computational fluid dynamics. Proc. S. D. Acad. Sci. 95, 119–124.
van der Laan, M.P., Kelly, M.C., Sørensen, N.N., 2017. A new k-epsilon model consistent with Monin-Obukhov similarity theory. Wind Energy 20, 479–489. https://doi.org/10.1002/we.2017.
Van Driest, E.R., 1956. On turbulent flow near a wall. J. Aeronaut. Sci. 23, 1007–1011. https://doi.org/10.2514/8.3713.
Whiteman, C.D., Haiden, T., Pospichal, B., Eisenbach, S., Steinacker, R., 2004. Minimum temperatures, diurnal temperature ranges, and temperature inversions in limestone sinkholes of different sizes and shapes. J. Appl. Meteorol. 43, 1224–1236. https://doi.org/10.1175/1520-0450(2004)043\%3C1224:MTDTRA\%3E2.0.CO;2.
Whiteman, C.D., Muschinski, A., Zhong, S., Fritts, D., Hoch, S.W., Hahnenberger, M., Yao, W., Hohreiter, V., Behn, M., Cheon, Y., Clements, C.B., Horst, T.W., Brown, W. O.J., Oncley, S.P., 2008. METCRAX 2006: meteorological experiments in Arizona's Meteor Crater. Bull. Am. Meteorol. Soc. 89, 1665–1680. https://doi.org/10.1175/2008BAMS2574.1.
Xie, B., 2016. Improved Vortex Method for LES Inflow Generation and Applications to Channel and Flat-Plate Flows.
Xu, G., Luxbacher, K.D., Ragab, S., Xu, J., Ding, X., 2017. Computational fluid dynamics applied to mining engineering: a review. Int. J. Min. Reclamat. Environ. 31, 251–275. https://doi.org/10.1080/17480930.2016.1138570.
Yakhot, V., Orszag, S.A., Yakhot, A., 1987. Heat transfer in turbulent fluids-I. pipe flow. Int. J. Heat Mass Tran. 30, 15–22. https://doi.org/10.1016/0017-9310(87)90057-3.
Yuan, Y., Yang, K., Du, C., Fu, X., 2017. Study on Schmidt number of pollutant diffusion in urban street atmosphere. Procedia Eng. 205, 1711–1717. https://doi.org/10.1016/j.proeng.2017.10.368.